Bulk properties of the system formed in Au+Au collisions at sqrt[s_{NN}]=14.5 GeV at the BNL STAR detector

J. Adam *et al.* (STAR Collaboration)

Bulk Properties of the System Formed in Au+Au Collisions at $\sqrt{s_{\mathrm{NN}}} = 14.5$ GeV at STAR

J. Adam,[6] L. Adamczyk,[2] J. R. Adams,[39] J. K. Adkins,[30] G. Agakishiev,[28] M. M. Aggarwal,[41] Z. Ahammed,[61] I. Alekseev,[3, 35] D. M. Anderson,[55] R. Aoyama,[58] A. Aparin,[28] D. Arkhipkin,[6] E. C. Aschenauer,[6] M. U. Ashraf,[57] F. Atetalla,[29] A. Attri,[41] G. S. Averichev,[28] V. Bairathi,[36] K. Barish,[10] A. J. Bassill,[10] A. Behera,[53] R. Bellwied,[20] A. Bhasin,[27] A. K. Bhati,[41] J. Bielcik,[14] J. Bielcikova,[38] L. C. Bland,[6] I. G. Bordyuzhin,[3] J. D. Brandenburg,[50, 6] A. V. Brandin,[35] J. Bryslawskyj,[10] I. Bunzarov,[28] J. Butterworth,[46] H. Caines,[64] M. Calderón de la Barca Sánchez,[8] D. Cebra,[8] I. Chakaberia,[29, 6] P. Chaloupka,[14] B. K. Chan,[9] F-H. Chang,[37] Z. Chang,[6] N. Chankova-Bunzarova,[28] A. Chatterjee,[61] S. Chattopadhyay,[61] J. H. Chen,[18] X. Chen,[49] J. Cheng,[57] M. Cherney,[13] W. Christie,[6] H. J. Crawford,[7] M. Csanád,[16] S. Das,[11] T. G. Dedovich,[28] I. M. Deppner,[19] A. A. Derevschikov,[43] L. Didenko,[6] C. Dilks,[42] X. Dong,[31] J. L. Drachenberg,[1] J. C. Dunlop,[6] T. Edmonds,[44] N. Elsey,[63] J. Engelage,[7] G. Eppley,[46] R. Esha,[53] S. Esumi,[58] O. Evdokimov,[12] J. Ewigleben,[32] O. Eyser,[6] R. Fatemi,[30] S. Fazio,[6] P. Federic,[38] J. Fedorisin,[28] Y. Feng,[44] P. Filip,[28] E. Finch,[52] Y. Fisyak,[6] L. Fulek,[2] C. A. Gagliardi,[55] T. Galatyuk,[15] F. Geurts,[46] A. Gibson,[60] K. Gopal,[23] D. Grosnick,[60] A. Gupta,[27] W. Guryn,[6] A. I. Hamad,[29] A. Hamed,[5] J. W. Harris,[64] L. He,[44] S. Heppelmann,[8] S. Heppelmann,[42] N. Herrmann,[19] L. Holub,[14] Y. Hong,[31] S. Horvat,[64] B. Huang,[12] H. Z. Huang,[9] S. L. Huang,[53] T. Huang,[37] X. Huang,[57] T. J. Humanic,[39] P. Huo,[53] G. Igo,[9] W. W. Jacobs,[25] C. Jena,[23] A. Jentsch,[6] Y. JI,[49] J. Jia,[6, 53] K. Jiang,[49] S. Jowzaee,[63] X. Ju,[49] E. G. Judd,[7] S. Kabana,[29] S. Kagamaster,[32] D. Kalinkin,[25] K. Kang,[57] D. Kapukchyan,[10] K. Kauder,[6] H. W. Ke,[6] D. Keane,[29] A. Kechechyan,[28] M. Kelsey,[31] Y. V. Khyzhniak,[35] D. P. Kikoła,[62] C. Kim,[10] T. A. Kinghorn,[8] I. Kisel,[17] A. Kisel,[62] M. Kocan,[14] L. Kochenda,[35] L. K. Kosarzewski,[14] L. Kramarik,[14] P. Kravtsov,[35] K. Krueger,[4] N. Kulathunga Mudiyanselage,[20] L. Kumar,[41] R. Kunnawalkam Elayavalli,[63] J. H. Kwasizur,[25] R. Lacey,[53] J. M. Landgraf,[6] J. Lauret,[6] A. Lebedev,[6] R. Lednicky,[28] J. H. Lee,[6] C. Li,[49] W. Li,[51] W. Li,[46] X. Li,[49] Y. Li,[57] Y. Liang,[29] R. Licenik,[38] T. Lin,[55] A. Lipiec,[62] M. A. Lisa,[39] F. Liu,[11] H. Liu,[25] P. Liu,[53] P. Liu,[51] T. Liu,[64] X. Liu,[39] Y. Liu,[55] Z. Liu,[49] T. Ljubicic,[6] W. J. Llope,[63] M. Lomnitz,[31] R. S. Longacre,[6] S. Luo,[12] X. Luo,[11] G. L. Ma,[51] L. Ma,[18] R. Ma,[6] Y. G. Ma,[51] N. Magdy,[12] R. Majka,[64] D. Mallick,[36] S. Margetis,[29] C. Markert,[56] H. S. Matis,[31] O. Matonoha,[14] J. A. Mazer,[47] K. Meehan,[8] J. C. Mei,[50] N. G. Minaev,[43] S. Mioduszewski,[55] D. Mishra,[36] B. Mohanty,[36] M. M. Mondal,[26] I. Mooney,[63] Z. Moravcova,[14] D. A. Morozov,[43] Md. Nasim,[22] K. Nayak,[11] J. M. Nelson,[7] D. B. Nemes,[64] M. Nie,[50] G. Nigmatkulov,[35] T. Niida,[63] L. V. Nogach,[43] T. Nonaka,[11] G. Odyniec,[31] A. Ogawa,[6] K. Oh,[45] S. Oh,[64] V. A. Okorokov,[35] B. S. Page,[6] R. Pak,[6] Y. Panebratsev,[28] B. Pawlik,[40] D. Pawlowska,[62] H. Pei,[11] C. Perkins,[7] R. L. Pintér,[16] J. Pluta,[62] J. Porter,[31] M. Posik,[54] N. K. Pruthi,[41] M. Przybycien,[2] J. Putschke,[63] A. Quintero,[54] S. K. Radhakrishnan,[31] S. Ramachandran,[30] R. L. Ray,[56] R. Reed,[32] H. G. Ritter,[31] J. B. Roberts,[46] O. V. Rogachevskiy,[28] J. L. Romero,[8] L. Ruan,[6] J. Rusnak,[38] O. Rusnakova,[14] N. R. Sahoo,[50] P. K. Sahu,[26] S. Salur,[47] J. Sandweiss,[64] J. Schambach,[56] W. B. Schmidke,[6] N. Schmitz,[33] B. R. Schweid,[53] F. Seck,[15] J. Seger,[13] M. Sergeeva,[9] R. Seto,[10] P. Seyboth,[33] N. Shah,[24] E. Shahaliev,[28] P. V. Shanmuganathan,[32] M. Shao,[49] F. Shen,[50] W. Q. Shen,[51] S. S. Shi,[11] Q. Y. Shou,[51] E. P. Sichtermann,[31] S. Siejka,[62] R. Sikora,[2] M. Simko,[38] J. Singh,[41] S. Singha,[29] D. Smirnov,[6] N. Smirnov,[64] W. Solyst,[25] P. Sorensen,[6] H. M. Spinka,[4] B. Srivastava,[44] T. D. S. Stanislaus,[60] M. Stefaniak,[62] D. J. Stewart,[64] M. Strikhanov,[35] B. Stringfellow,[44] A. A. P. Suaide,[48] T. Sugiura,[58] M. Sumbera,[38] B. Summa,[42] X. M. Sun,[11] Y. Sun,[49] Y. Sun,[21] B. Surrow,[54] D. N. Svirida,[3] P. Szymanski,[62] A. H. Tang,[6] Z. Tang,[49] A. Taranenko,[35] T. Tarnowsky,[34] J. H. Thomas,[31] A. R. Timmins,[20] D. Tlusty,[13] T. Todoroki,[6] M. Tokarev,[28] C. A. Tomkiel,[32] S. Trentalange,[9] R. E. Tribble,[55] P. Tribedy,[6] S. K. Tripathy,[26] O. D. Tsai,[9] B. Tu,[11] Z. Tu,[6] T. Ullrich,[6] D. G. Underwood,[4] I. Upsal,[50, 6] G. Van Buren,[6] J. Vanek,[38] A. N. Vasiliev,[43] I. Vassiliev,[17] F. Videbæk,[6] S. Vokal,[28] S. A. Voloshin,[63] F. Wang,[44] G. Wang,[9] P. Wang,[49] Y. Wang,[11] Y. Wang,[57] J. C. Webb,[6] L. Wen,[9] G. D. Westfall,[34] H. Wieman,[31] S. W. Wissink,[25] R. Witt,[59] Y. Wu,[29] Z. G. Xiao,[57] G. Xie,[12] W. Xie,[44] H. Xu,[21] N. Xu,[31] Q. H. Xu,[50] Y. F. Xu,[51] Z. Xu,[6] C. Yang,[50] Q. Yang,[50] S. Yang,[6] Y. Yang,[37] Z. Yang,[11] Z. Ye,[46] Z. Ye,[12] L. Yi,[50] K. Yip,[6] I. -K. Yoo,[45] H. Zbroszczyk,[62] W. Zha,[49] D. Zhang,[11] L. Zhang,[11] S. Zhang,[49] S. Zhang,[51] X. P. Zhang,[57] Y. Zhang,[49] Z. Zhang,[51] J. Zhao,[44] C. Zhong,[51] C. Zhou,[51] X. Zhu,[57] Z. Zhu,[50] M. Zurek,[31] and M. Zyzak[17]

(STAR Collaboration)

[1] *Abilene Christian University, Abilene, Texas 79699*
[2] *AGH University of Science and Technology, FPACS, Cracow 30-059, Poland*
[3] *Alikhanov Institute for Theoretical and Experimental Physics, Moscow 117218, Russia*
[4] *Argonne National Laboratory, Argonne, Illinois 60439*
[5] *American Univerisity of Cairo, Cairo, Egypt*

[6]*Brookhaven National Laboratory, Upton, New York 11973*
[7]*University of California, Berkeley, California 94720*
[8]*University of California, Davis, California 95616*
[9]*University of California, Los Angeles, California 90095*
[10]*University of California, Riverside, California 92521*
[11]*Central China Normal University, Wuhan, Hubei 430079*
[12]*University of Illinois at Chicago, Chicago, Illinois 60607*
[13]*Creighton University, Omaha, Nebraska 68178*
[14]*Czech Technical University in Prague, FNSPE, Prague 115 19, Czech Republic*
[15]*Technische Universität Darmstadt, Darmstadt 64289, Germany*
[16]*Eötvös Loránd University, Budapest, Hungary H-1117*
[17]*Frankfurt Institute for Advanced Studies FIAS, Frankfurt 60438, Germany*
[18]*Fudan University, Shanghai, 200433*
[19]*University of Heidelberg, Heidelberg 69120, Germany*
[20]*University of Houston, Houston, Texas 77204*
[21]*Huzhou University, Huzhou, Zhejiang 313000*
[22]*Indian Institute of Science Education and Research (IISER), Berhampur 760010 , India*
[23]*Indian Institute of Science Education and Research, Tirupati 517507, India*
[24]*Indian Institute Technology, Patna, Bihar, India*
[25]*Indiana University, Bloomington, Indiana 47408*
[26]*Institute of Physics, Bhubaneswar 751005, India*
[27]*University of Jammu, Jammu 180001, India*
[28]*Joint Institute for Nuclear Research, Dubna 141 980, Russia*
[29]*Kent State University, Kent, Ohio 44242*
[30]*University of Kentucky, Lexington, Kentucky 40506-0055*
[31]*Lawrence Berkeley National Laboratory, Berkeley, California 94720*
[32]*Lehigh University, Bethlehem, Pennsylvania 18015*
[33]*Max-Planck-Institut für Physik, Munich 80805, Germany*
[34]*Michigan State University, East Lansing, Michigan 48824*
[35]*National Research Nuclear University MEPhI, Moscow 115409, Russia*
[36]*National Institute of Science Education and Research, HBNI, Jatni 752050, India*
[37]*National Cheng Kung University, Tainan 70101*
[38]*Nuclear Physics Institute of the CAS, Rez 250 68, Czech Republic*
[39]*Ohio State University, Columbus, Ohio 43210*
[40]*Institute of Nuclear Physics PAN, Cracow 31-342, Poland*
[41]*Panjab University, Chandigarh 160014, India*
[42]*Pennsylvania State University, University Park, Pennsylvania 16802*
[43]*NRC "Kurchatov Institute", Institute of High Energy Physics, Protvino 142281, Russia*
[44]*Purdue University, West Lafayette, Indiana 47907*
[45]*Pusan National University, Pusan 46241, Korea*
[46]*Rice University, Houston, Texas 77251*
[47]*Rutgers University, Piscataway, New Jersey 08854*
[48]*Universidade de São Paulo, São Paulo, Brazil 05314-970*
[49]*University of Science and Technology of China, Hefei, Anhui 230026*
[50]*Shandong University, Qingdao, Shandong 266237*
[51]*Shanghai Institute of Applied Physics, Chinese Academy of Sciences, Shanghai 201800*
[52]*Southern Connecticut State University, New Haven, Connecticut 06515*
[53]*State University of New York, Stony Brook, New York 11794*
[54]*Temple University, Philadelphia, Pennsylvania 19122*
[55]*Texas A&M University, College Station, Texas 77843*
[56]*University of Texas, Austin, Texas 78712*
[57]*Tsinghua University, Beijing 100084*
[58]*University of Tsukuba, Tsukuba, Ibaraki 305-8571, Japan*
[59]*United States Naval Academy, Annapolis, Maryland 21402*
[60]*Valparaiso University, Valparaiso, Indiana 46383*
[61]*Variable Energy Cyclotron Centre, Kolkata 700064, India*
[62]*Warsaw University of Technology, Warsaw 00-661, Poland*
[63]*Wayne State University, Detroit, Michigan 48201*
[64]*Yale University, New Haven, Connecticut 06520*

We report systematic measurements of bulk properties of the system created in Au+Au collisions at $\sqrt{s_{NN}} = 14.5$ GeV recorded by the STAR detector at the Relativistic Heavy Ion Collider (RHIC). The transverse momentum spectra of $\pi^{\pm}$, $K^{\pm}$ and $p(\bar{p})$ are studied at mid-rapidity ($|y| < 0.1$) for nine centrality intervals. The centrality, transverse momentum (p_T), and pseudorapidity (η)

dependence of inclusive charged particle elliptic flow (v_2), and rapidity-odd charged particles directed flow (v_1) results near mid-rapidity are also presented. These measurements are compared with the published results from Au+Au collisions at other energies, and from Pb+Pb collisions at $\sqrt{s_{NN}} =$ 2.76 TeV. The results at $\sqrt{s_{NN}} =$ 14.5 GeV show similar behavior as established at other energies and fit well in the energy dependence trend. These results are important as the 14.5 GeV energy fills the gap in μ_B, which is of the order of 100 MeV, between $\sqrt{s_{NN}} =$11.5 and 19.6 GeV. Comparisons of the data with UrQMD and AMPT models show poor agreement in general.

I. INTRODUCTION

According to quantum chromodynamics (QCD), at very high temperature and/or at high density, a deconfined phase of quarks and gluons is expected to be present. At low temperature and low density, quarks and gluons are confined inside hadrons. The exploration of the QCD phase diagram, in the plane of temperature (T) and the baryon chemical potential (μ_B), is one of the primary objectives of high-energy heavy-ion collision experiments [1–7]. During the initial stages of Au+Au collisions at top RHIC energies, there is evidence of a phase with partonic degrees of freedom [1–4, 8–13], which later transits into one with hadronic degrees of freedom [14–17]. Relevant evidence includes strong suppression of high transverse momentum (p_T) hadron production in Au+Au collisions relative to $p + p$ collisions [1–4, 8–11], large elliptic flow (v_2) for hadrons containing light as well as strange and charm valence quarks, and the difference between baryon and meson v_2 at intermediate p_T [18].

At $\mu_B = 0$, the phase transition is a cross-over. This region is well described by lattice QCD calculations [19, 20]. At larger μ_B, a first-order phase transition is suggested by lattice QCD [21] and various QCD-based models [22–25]. The end point of the first-order phase transition in the T,μ_B plane is the QCD critical point [26, 27]. To discover this critical point and to search for the phase boundary, the Beam Energy Scan (BES-I) program [28–31] was carried out by RHIC in the years 2010 and 2011. Au+Au collisions were recorded at $\sqrt{s_{NN}} =$ 7.7, 11.5, 19.6, 27, and 39 GeV. In the year 2014, another Au+Au collision energy at $\sqrt{s_{NN}} =$ 14.5 GeV was added to this BES-I program to bridge the 100 MeV gap in μ_B [32] between the beam energies of 11.5 and 19.6 GeV.

In this paper, we present bulk properties of the system, namely p_T spectra (π,K,p), dN/dy, $\langle p_T \rangle$, particle ratios, kinetic freeze-out properties, rapidity-odd directed flow v_1 (charged hadrons), and v_2 (charged hadrons) in Au+Au collisions at $\sqrt{s_{NN}} =$ 14.5 GeV. A systematic study of these observables as a function of p_T, pseudorapidity (η), and collision centrality is discussed in detail. Comparisons of the results with those in Au+Au collisions at other RHIC energies and with Pb+Pb collisions at $\sqrt{s_{NN}} =$ 2.76 TeV are presented. The results are also compared to model calculations, namely UrQMD (a hadronic transport model) [33] and AMPT (a transport model with both hadronic and partonic interactions) [34]. Earlier measurements suggest that systems at lower energies, such as 7.7 and 11.5 GeV, behave like hadron gases, while at energies of 19.6 GeV and above, they show par-

tonic behavior [35–44]. The Au+Au collisions at $\sqrt{s_{NN}} =$ 14.5 GeV, lying between these two energies, allow studies of the interplay between hadronic and partonic phases.

II. EXPERIMENT AND DATA ANALYSIS

A. STAR Detector

This paper reports the results for Au+Au collisions at $\sqrt{s_{NN}} =$ 14.5 GeV taken by the STAR detector [45] at RHIC under the BES-I program. The selected minimum-bias data triggered by the Beam Beam Counters (BBCs) [46, 47] are used for this analysis. The BBCs are two scintillator-based detectors situated on both sides of the center of STAR at pseudorapidity $3.8 < |\eta| < 5.2$ with full azimuthal coverage. The detector primarily used for tracking is the Time Projection Chamber (TPC) [48]. The TPC is a gas detector filled with P10 gas (90% Argon and 10% Methane). It operates at a pressure of 2 mbar above atmospheric pressure in a constant magnetic field of 0.5 Tesla in the longitudinal (z) direction. The TPC has an acceptance of $|\eta| < 1$ in pseudorapidity and 2π in azimuth. Through ionization energy loss ($\langle dE/dx \rangle$) measurements of the particles traversing the TPC gas, different particles can be identified. The Time of Flight (TOF) detector is also used for particle identification [49]. The TOF uses Multi Resistive Plate Chamber (MRPC) technology. It provides full azimuthal coverage and has a pseudorapidity acceptance of $|\eta| < 0.9$.

B. Event Selection

The primary vertex of each event is determined by finding the best common point from where most of the tracks originate. Along the beam direction, a vertex position cut of $|V_z| < 30$ cm is applied to select events for the spectra analysis. For v_1 and v_2 analyses, a broader cut of $|V_z| < 70$ cm is applied to obtain reasonable statistics. In Au+Au collisions at 14.5 GeV, the mean vertex position for all events is centred at $(0, -0.89)$ cm in x-y plane. A radial vertex position cut (defined by $V_r = \sqrt{V_x^2 + V_y^2}$) of $V_r < 1$ cm from the centre is applied to reject interactions involving the beam pipe. After these event cuts, the number of events analyzed for π, K, p spectra is nearly 10

million, while the number of events for inclusive charged particle v_1 and v_2 analyses is about 17 million.

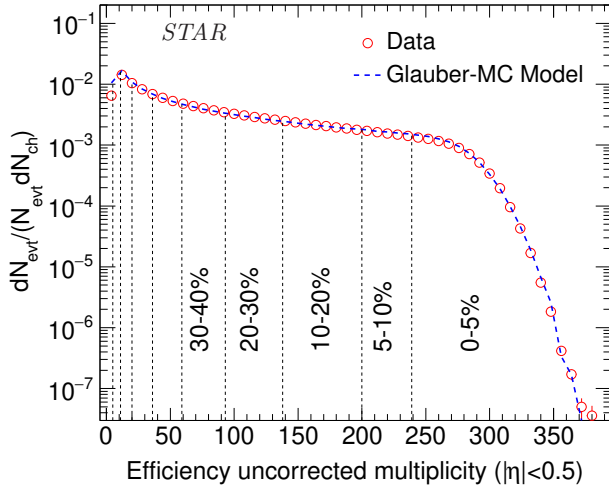### C.   Centrality Selection

FIG. 1. Uncorrected charged-particle multiplicity distribution (open circles) measured in the TPC within $|\eta| < 0.5$ in Au+Au collisions at $\sqrt{s_{NN}} = 14.5$ GeV. The blue dashed line represents the charged particle multiplicity distribution from a MC Glauber model [50]. The vertical dashed lines represent the centrality selection criteria used.

The uncorrected charged-particle multiplicity distribution is compared and fitted with Glauber Monte-Carlo (MC) simulations as shown in Fig. 1. The detailed procedure to obtain the simulated multiplicity using Glauber Monte-Carlo is similar to that described in [50]. The minimum-bias trigger events are divided into nine centrality classes: 0–5%, 5–10%, 10–20%, 20–30%, 30–40%, 40–50%, 50–60%, 60–70% and 70–80%. The quoted fractions are in terms of the total cross section obtained from the simulated events with the Glauber model. In addition, quantities such as average number of participating nucleons $\langle N_{\text{part}} \rangle$, number of binary collisions $\langle N_{\text{coll}} \rangle$ etc. are estimated and are listed in Table II.

D.   Track Selection

Details of the track cuts are tabulated in Table III. The distance of closest approach (DCA) of tracks to the primary vertex is required to be less than 3 cm to suppress tracks from secondary decays. In the spectra analysis, the number of fit points associated with a track has to be 25 or more out of a maximum possible 45 hits in the TPC, while for v_1 and v_2 analyses, 15 or more hits are required. The cuts in these analyses are the same

as the standard cuts established in previous STAR published papers. The fraction of fit points on a track is required to be greater than 52% of the total possible hits to avoid split tracks. To have a good ionization energy loss $\langle dE/dx \rangle$ resolution for tracks, the number of TPC hits used to determine $\langle dE/dx \rangle$ is required to be 15 or more. The spectra results are obtained for tracks within the rapidity window $|y| < 0.1$. Inclusive charged particle v_1 and v_2 analyses are carried out using tracks within pseudorapidity $|\eta| < 1$.

E.   Particle Identification

Particle identification in the TPC is carried out by measuring the truncated mean of the ionization energy loss ($\langle dE/dx \rangle$) for each of the selected tracks. The measured $\langle dE/dx \rangle$ of the charged particles as a function of rigidity, p/q (momentum per charge in units of the electron charge) is presented in panel (a) of Fig. 2. The solid curves represent theoretical values predicted by the Bichsel formula [51]. The TPC can identify pions, kaons and protons with relatively low momentum, but the separate bands start merging at higher momentum. The pions and kaons can be identified up to p_T of 0.8 GeV/c and protons up to 1.0 GeV/c.

For particle identification at relatively higher momentum, the TOF detector is utilized. In this analysis, TOF information is used for particle identification in the p_T range 0.4–2.0 GeV/c (0.5–2.0 GeV/c) for pions and kaons (protons). Panel (b) of Fig. 2 shows the characteristic plot for TOF in which the inverse of particle velocity in units of the speed of light, $1/\beta$, is plotted as a function of p/q. The solid lines are the expected values for pions, kaons and protons.

The $\langle dE/dx \rangle$ distribution for a specific particle type in the TPC does not have a Gaussian shape [52]. It has been demonstrated that a more appropriate Gaussian variable for a given choice of particle type is the z-variable [52], defined as

$$z_X = \ln \left(\frac{\langle dE/dx \rangle}{\langle dE/dx \rangle_X^B} \right), \qquad (1)$$

where X is the particle type ($e^{\pm}$, $\pi^{\pm}$, $K^{\pm}$, p or $\bar{p}$ in the present analysis) and $\langle dE/dx \rangle_X^B$ is the corresponding prediction of $\langle dE/dx \rangle$ from the Bichsel function [51]. The z_X distribution for each particle type is expected to peak at 0.

The z_X distributions are constructed for a particular choice of particle, for a given p_T range within rapidity $|y| < 0.1$. Panel (a) of Fig. 3 shows the z_{π} distribution for positively charged tracks of $0.30 < p_T < 0.35$ GeV/c. The distributions are then fitted by a multi-Gaussian function to extract the raw yield. The area under the Gaussian curve for the particle under consideration gives
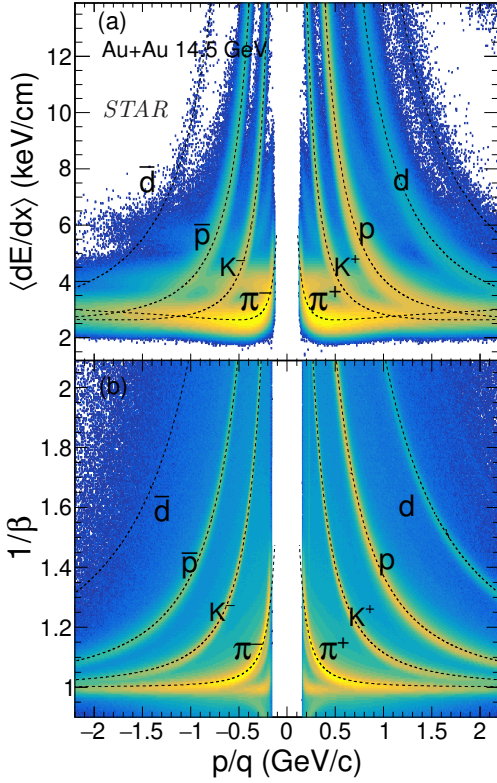
FIG. 2. Panel (a): The $\langle dE/dx \rangle$ distribution of charged particles from the TPC as a function of momentum/charge for Au+Au collisions at $\sqrt{s_{NN}} = 14.5$ GeV. The curves represent the expected mean values of $\langle dE/dx \rangle$ for the corresponding particle species. Panel (b): $1/\beta$ as a function of momentum/charge from TOF in Au+Au collisions at $\sqrt{s_{NN}} = 14.5$ GeV. The curves represent the expected values of $1/\beta$ for the indicated particle species.

the yield of that particle for that p_T range. As can be noticed from Fig. 3, the pion peak is slightly shifted towards the negative side of zero on the z_π axis. This could be due to issues related to calibration. However, any shift of the pion peak from zero does not have an impact on the raw yield value. This method is applicable for low p_T values, up to the point where the distributions for pions, kaons and protons are well separated. For higher p_T, where the distributions start to overlap, the widths of the Gaussian distributions are constrained according to the values at lower p_T. Following a similar procedure for each particle type, raw yields are extracted for different p_T ranges in nine centrality classes.

The raw yields from TOF are obtained using the m^2 variable defined as

$$m^2 = p^2 \left(\frac{c^2 T^2}{L^2} - 1 \right), \qquad (2)$$

where p, T, L, and c are particle momentum, Time-of-flight, path length of the particle, and the speed of light, respectively. Within $|y| < 0.1$, the m^2 distribu-

tions are obtained for the particle of interest in a given p_T range, and one example is shown in panel (b) of Fig. 3 for the case of π^+. To extract the raw yields using m^2 distributions, we follow the same procedure as done in Refs. [32, 53]. In this method, the m^2 distributions from data are fitted using the predicted m^2 distributions. The predicted m^2 distribution is generated by the measured time-of-flight from experimental data, thus including the TOF detector response behavior, for a given dE/dx-identified particle. It is observed that the predicted m^2 distributions do not change much with p_T and can be extended to higher p_T where dE/dx identification is limited. These predicted m^2 distributions of pions, kaons and protons are used simultaneously to fit the measured m^2 distributions to obtain the raw yield as shown for π^+ in panel (b) of Fig. 3 for p_T range 0.5–0.6 GeV/c. In this way, the raw yields are obtained for all p_T bins, centralities and different particles.

F. Flow Analysis

The azimuthal distribution of emitted particles with respect to the reaction plane can be decomposed in a Fourier series [54]. The harmonic coefficients (v_n) in this expansion are defined as,

$$v_n = \langle \cos n(\phi - \Psi_R) \rangle. \qquad (3)$$

Here, angle brackets denote an average over all particles in all events for a given p_T or η bin, and Ψ_R is the azimuth of the reaction plane angle. The first harmonic coefficient is called the directed flow (v_1), while the second is called the elliptic flow (v_2). Since the Ψ_R is unknown experimentally, it is estimated from

$$\Psi_n = \frac{1}{n} \tan^{-1} \left(\frac{\sum\limits_{i=1}^{N} w_i \sin(n\phi_i)}{\sum\limits_{i=1}^{N} w_i \cos(n\phi_i)} \right), \qquad (4)$$

where Ψ_n is n^{th}-order event plane azimuth, w_i are weights, and N is the total number of particles in an event used for the event plane calculation [54]. The observed v_n^{obs} is calculated with respect to the reconstructed event plane using

$$v_n^{\mathrm{obs}} = \langle \cos n(\phi - \Psi_n) \rangle. \qquad (5)$$

The observed v_n are then corrected for event plane resolution [55, 56].

Two types of event plane angles are used in this analysis: the TPC event plane [50] and the BBC event plane [57]. In the TPC event plane method, a second-order event plane angle (Ψ_2) is reconstructed from TPC tracks at mid-rapidity ($|\eta| < 1$). To reduce nonflow contributions, we utilize the η-sub method, with an additional η-gap of 0.1 between the sub-events, and then average the results from the two sub-events [50]. In the
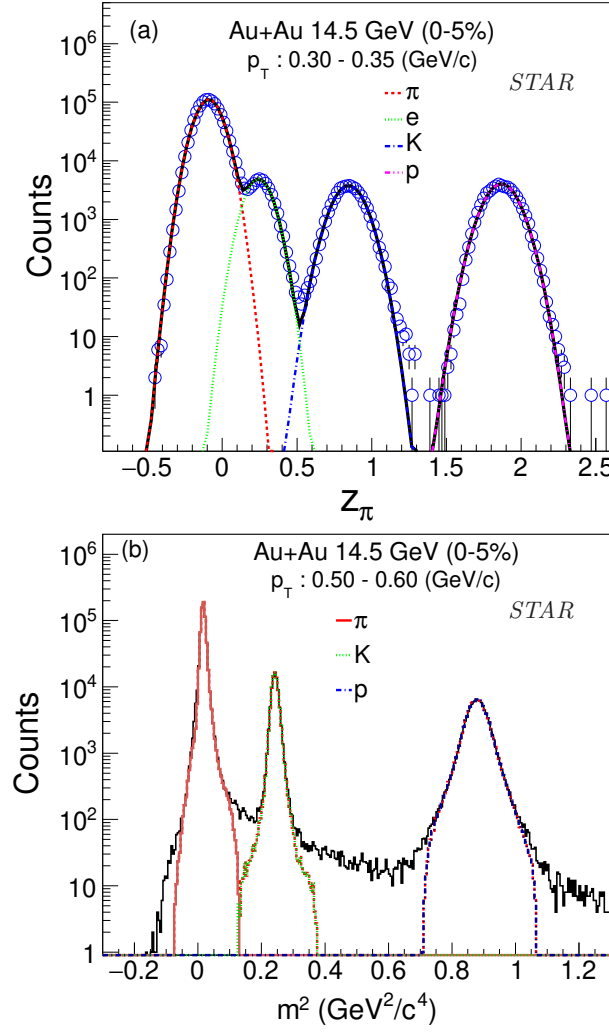
FIG. 3. Panel (a): The z_π distribution at midrapidity ($|y| < 0.1$) for the p_T range 0.30–0.35 GeV/c in 0–5% central Au+Au collisions at $\sqrt{s_{NN}} = 14.5$ GeV. The curves are Gaussian fits representing contributions from pions (dashed red), electrons (dotted green), kaons (dash-dotted blue), and protons (dash-dot-dotted magenta). The uncertainties are statistical only. Panel (b): The m^2 distributions used to obtain the raw yields from TOF for π^+ within $|y| < 0.1$ in the p_T range 0.5–0.6 GeV/c. These distributions are for 0–5% centrality in Au+Au collisions at $\sqrt{s_{NN}} = 14.5$ GeV. The curves are fits to the m^2 distribution, representing contributions from pions (red), kaons (blue) and protons (magenta).

BBC event plane method, a first-order event plane (Ψ_1), reconstructed using the hits in both BBC detectors in opposite hemispheres ($3.8 < |\eta| < 5.2$), is used to calculate v_1 and v_2. Re-centering and shift techniques were applied for each η hemisphere independently to flatten the TPC event plane and BBC event plane [54]. More details about these methods can be found in a previous publication [50].

In addition to the event plane method, the multi-particle correlation method [58, 59] is used to calculate v_2 of charged particles. In this method, the reference flow (e.g., integrated over p_T) can be estimated both from two- and four-particle cumulants:

$$v_n\{2\} = \sqrt{c_n\{2\}}, \qquad (6)$$

$$v_n\{4\} = \sqrt[4]{-c_n\{4\}}. \qquad (7)$$

Here $c_n\{2\}$ and $c_n\{4\}$ are two- and four-particle cumulants. The two- and four-particle cumulants without detector bias then can be formulated as

$$c_n\{2\} = \langle\langle e^{in(\phi_1 - \phi_2)}\rangle\rangle, \qquad (8)$$

$$c_n\{4\} = \langle\langle e^{in(\phi_1 + \phi_2 - \phi_3 - \phi_4)}\rangle\rangle - 2 \times \langle\langle e^{in(\phi_1 - \phi_2)}\rangle\rangle. \, (9)$$

Here, double angle brackets denote an average over all events. More details about these methods are presented in [50].

III. CORRECTION FACTORS

A. Monte-Carlo Embedding Technique

Several correction factors for the p_T spectra are calculated from MC simulations known as the embedding technique. The method is outlined below and more details can be found in Refs. [28, 32, 60]. For a given particle, MC tracks having flat rapidity and p_T distributions are simulated in the STAR detector using GEANT3. Those simulated tracks are then embedded into real events at the raw data level. The multiplicity of embedded tracks in any real event is no more than 5% of the measured real charged particle multiplicity of that event. These embedded tracks are reconstructed in the same manner as the real data reconstruction. The embedding sample is used to calculate various correction factors such as tracking efficiency and acceptance, and energy loss correction as discussed below.

B. Energy Loss Correction

The TPC track reconstruction algorithm assumes the pion mass for each particle when correcting for multiple Coulomb scattering and energy loss in the TPC gas, which mostly affect particles of low momenta. Therefore, a correction for momentum loss by heavier particles like $K^{\pm}$ and $p(\bar{p})$ is needed. This correction is obtained from MC simulation or embedding techniques. The distribution of momentum difference between reconstructed momentum p_T^{REC} and initial momentum p_T^{MC} as a function of p_T^{REC} gives the amount of energy loss correction for each track. The relevant plot for Au+Au collisions at $\sqrt{s_{\mathrm{NN}}} = 14.5$ GeV, showing the p_T dependence of energy loss, is presented in Fig. 4 for pions (left), kaons (middle) and protons (right). The red curve represents a functional fit to the data points in the case of kaons and protons,

$$f(p_T) = A + B \left(1 + \frac{C}{p_T^2} \right)^D, \qquad (10)$$

where A, B, C and D are fit parameters. This energy loss fraction is the same for all centrality classes for a particular particle type. All the results shown in this paper have been corrected for this energy loss effect.

C. Tracking Efficiency and Acceptance

A correction for detector efficiency and acceptance needs to be applied to the p_T spectra of analyzed particles. This correction factor is obtained from the embedding technique described above. The combined tracking efficiency and acceptance is the ratio of the distribution of reconstructed to original Monte-Carlo tracks as a function of p_T in the rapidity range of interest. This functional dependence of combined tracking efficiency and acceptance on p_T is presented in Fig. 5 for reconstructed pions (left), kaons (middle), and protons (right) in Au+Au collisions at $\sqrt{s_{\mathrm{NN}}} = 14.5$ GeV. The curves represent the functional fit of the form $p_0 \exp[-(p_1/p_T)^{p_2}]$, used to parameterize the efficiency. This correction factor is thus calculated for each particle type in nine centrality classes and each p_T spectrum is divided by this fraction.

D. TOF Matching Efficiency

The TOF detectors form a curved cylindrical surface surrounding the TPC and have a reduced geometric acceptance compared to the TPC. Circumstances arise where TPC tracks are not detected in TOF, especially at low momentum, either because the track is out of the TOF acceptance or because of the TOF inefficiency. As a result, the yield of particles identified by TOF needs to be corrected, in addition to the TPC track reconstruction efficiency. This is referred to as the TOF matching efficiency or TOF particle identification efficiency for TPC tracks. This efficiency is calculated from the STAR data as the ratio of the number of tracks detected in TOF to the total number of tracks in the TPC within the acceptance under study. It is shown as a function of p_T in Fig. 6 for pions (left), kaons (middle) and protons (right) in Au+Au collisions at $\sqrt{s_{\mathrm{NN}}} = 14.5$ GeV for 0–5% centrality. The raw yields obtained using TOF are divided by the matching efficiency for each centrality, p_T range, and for each particle type.

E. Pion Background Correction

The measured pions get a contribution from the feed-down of weak decays, muon contamination, and background pions produced in the detector material. Therefore, it is important to remove these background contributions from the total pion yield. To obtain this correction, we used the same approach as done in Refs. [32, 60]. The Monte-Carlo simulated events are generated by HIJING [61] and are processed through the STAR detector simulated by GEANT3 [62]. These events are reconstructed in the same manner as real data. In the MC sample, the pion background fraction is estimated since different contributions to the total pion yield are known. The pion background fraction decreases exponentially with p_T. Its value at low $p_T (=0.225$ GeV/$c)$ is $\sim 16\%$ and becomes negligible above 0.6 GeV/c. It shows negligible centrality dependence, hence the same correction is applied for all centrality classes.
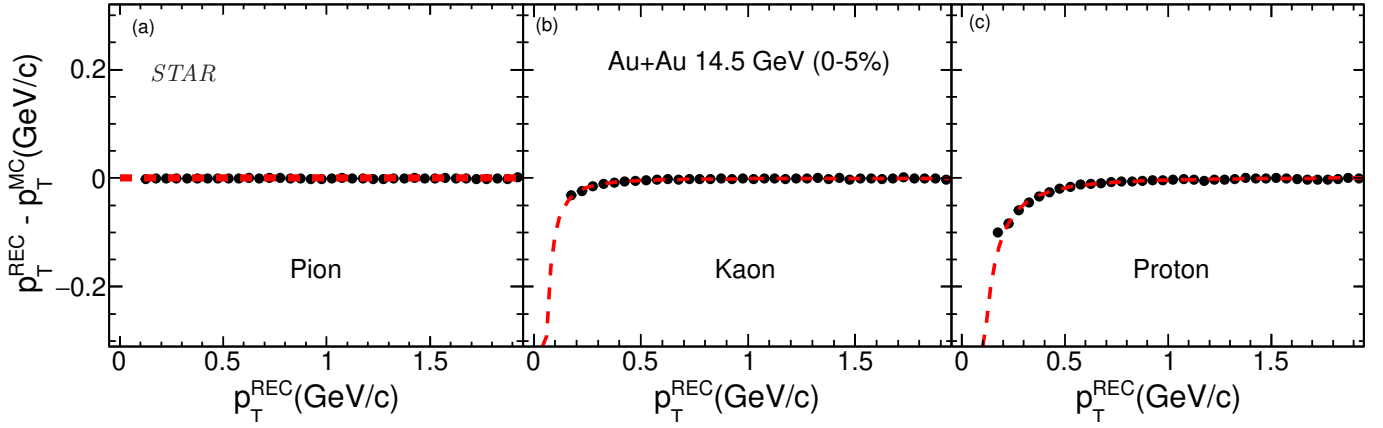
FIG. 4. The p_T difference of reconstructed momentum p_T^{REC} and MC momentum p_T^{MC} as a function of p_T^{REC} for (a) pions, (b) kaons and (c) protons in 0-5% central Au+Au collisions at $\sqrt{s_{\mathrm{NN}}} = 14.5$ GeV. The red curves represent the functional fit of the form $f(p_T) = A + B\left(1 + \frac{C}{p_T^2}\right)^D$.
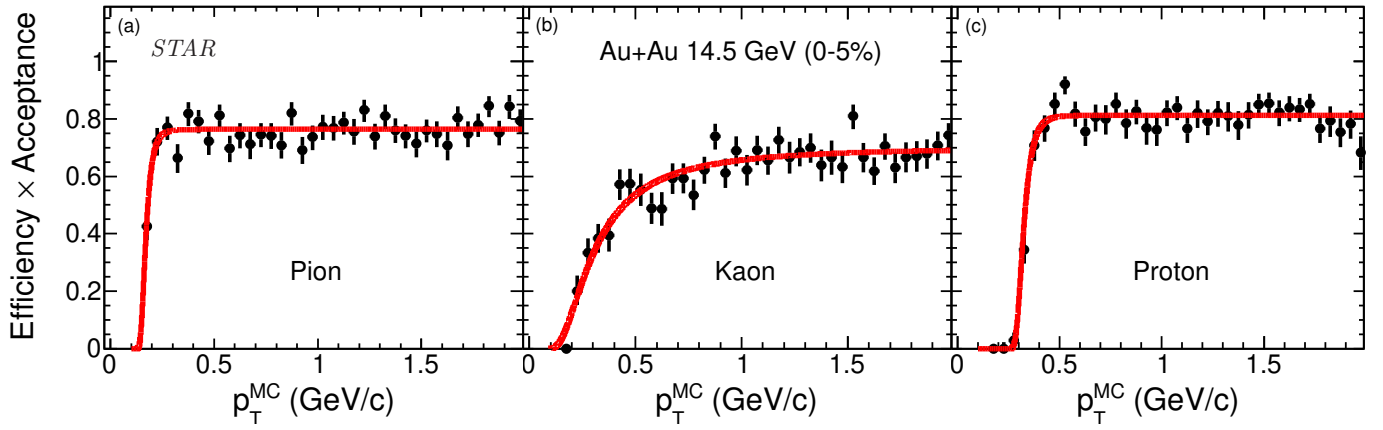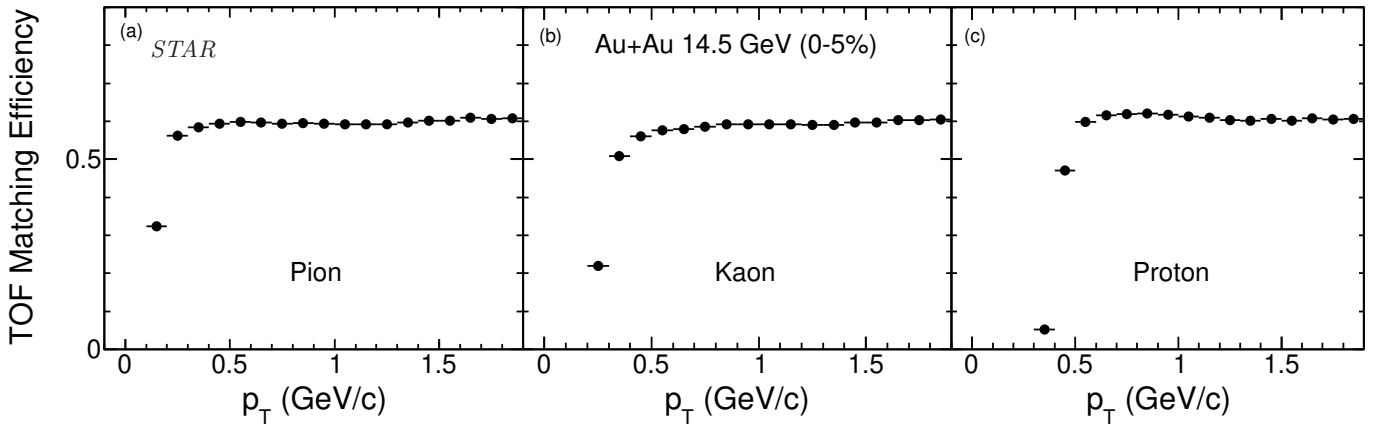

FIG. 5. The combined tracking efficiency and acceptance as a function of p_T calculated from the Monte-Carlo embedding technique for reconstructed (a) pions, (b) kaons, and (c) protons at midrapidity ($|y| < 0.1$) for 0-5% Au+Au collisions at $\sqrt{s_{\mathrm{NN}}} = 14.5$ GeV. The curves represent the functional fit of the form $p_0 \exp[-(p_1/p_T)^{p_2}]$.

FIG. 6. TOF matching efficiency as a function of p_T for (a) pions, (b) kaons and (c) protons at midrapidity ($|y| < 0.1$) in 0-5% Au+Au collisions at $\sqrt{s_{\mathrm{NN}}} = 14.5$ GeV.

F. Proton Background Correction

The yield of protons has a significant contribution from background protons coming from interactions of highly energetic particles with the detector material. In order to estimate the proton background fraction, we follow the same procedure as used in Refs. [32, 60, 63]. This fraction is estimated by comparing the proton and antiproton DCA distributions obtained from real data. The difference between the proton and antiproton DCA distribution gives the estimate of proton background contribution. The proton background fraction decreases as a function of p_T and decreases from peripheral to central collisions. At $p_T = 0.60$–0.65 GeV/c, its typical value is about 40% in peripheral collisions and 2% in central collisions. For minimum bias collisions, proton background at low p_T is around 15% and becomes almost negligible for $p_T > 1.2$ GeV/c. The (anti)protons also have a contribution of feed-down from weak decays of hyperons, which include particles like Σ which has not been measured. Contrary to pions, the analysis cut of DCA < 3 cm includes almost all daughter particles from hyperon decays [64, 65]. Thus, (anti)proton yields presented here are all inclusive similar to those at other RHIC energies [32, 60].

IV. SYSTEMATIC UNCERTAINTIES

To estimate the size of systematic uncertainties associated with the p_T spectra of the particles under study, we vary the event and track cuts, and the quality of fits to $\langle dE/dx \rangle$ measurements. The following parameters are varied: the event V_z range (from $|V_z| < 30$ cm to $|V_z| < 50$ cm), track cuts like DCA (from 3 cm to 2 cm), number of fit points (from 25 to 20), and number of $\langle dE/dx \rangle$ points (from 15 to 10). We have also varied the fit range for the z distribution and the PID selection (using $\langle dE/dx \rangle$) cut of a given particle used for the predicted m^2 distribution.

TABLE I. Systematic uncertainties related to π, K and $p(\bar{p})$ integrated particle yields in Au+Au collisions at $\sqrt{s_{\mathrm{NN}}} = 14.5$ GeV.

	π	K	$p(\bar{p})$
V_z	1%	1%	1%
Track Cuts	4%	4%	6%
PID	6%	8%	7%
Extrapolation	5%	4%	6%
Corrections	5%	5%	5%
Proton Background	-	-	5–6%
Total	10%	10%	12%

Apart from these systematic uncertainties for the case of p_T spectra, an additional error of 5% is added in quadrature due to detector tracking efficiency and acceptance [32, 60, 65]. The pion feed-down correction and the proton background fraction also contribute to the systematic uncertainty; however, the former is negligible and the latter contributes about 5–6% only at low p_T. All the sources of systematic uncertainty are added in quadrature and are tabulated in Table I. The total systematic uncertainties on pion, kaon and proton yields are 10%, 10% and 12%, respectively.

The calculation of p_T integrated particle yields (dN/dy) and $\langle p_T \rangle$ requires a fitting function to extrapolate the p_T spectra to the unmeasured p_T region. Thus, another important source of systematic uncertainty in dN/dy and $\langle p_T \rangle$ is extrapolation. For pions, kaons and protons, the default fit functions used to extract yields are Bose-Einstein, m_T-exponential, and double exponential, respectively. To estimate the systematic uncertainty, these fit functions for pions, kaons and protons are changed to p_T-exponential, Boltzmann and m_T-exponential functions, respectively. The relevant functional forms are

- Bose-Einstein: $\propto 1/(\exp(m_T/T_{\mathrm{BE}}) - 1)$

- p_T-exponential: $\propto \exp(-p_T/T_{p_T})$

- m_T-exponential: $\propto \exp(-m_T/T_{m_T})$

- Boltzmann: $\propto m_T \exp(-m_T/T_B)$

- Double-exponential: $A\,e^{-p_T^2/T_1^2} + B\,e^{-p_T^2/T_2^2}$

The systematic uncertainty on mean p_T mainly comes from the errors associated with extrapolation of p_T spectra. The fitting range of the fit function also affects the value of $\langle p_T \rangle$, which is included as a source of systematic uncertainty. The systematic uncertainty on $\langle p_T \rangle$ for pions, kaons and protons is 5%, 2% and 6%, respectively.

The systematic uncertainty on integrated particle ratios is calculated from the systematic uncertainty on dN/dy. The systematic uncertainty due to tracking efficiency cancels in particle ratios. The error associated with extrapolation mostly cancels in the case of particle to antiparticle ratios, but does not cancel for the ratios of different particle species.

The Blast-Wave fit [66] to particle p_T spectra provides the kinetic freeze-out parameters. The point-to-point systematic uncertainty associated with the p_T spectra propagates to the systematic uncertainties on the kinetic freeze-out parameters. The p_T ranges used for fitting also affect the results. These variations are included in the systematic uncertainty on kinetic freeze-out parameters.

The systematic uncertainties for v_1 and v_2 measurements are estimated by varying event and track cut parameters from their default values. The z-position of the primary vertex is varied between 60 and 80 cm. The DCA of the primary tracks is varied between 2.0 cm and 3.0 cm. The number of fit points is varied from 18 to 25.
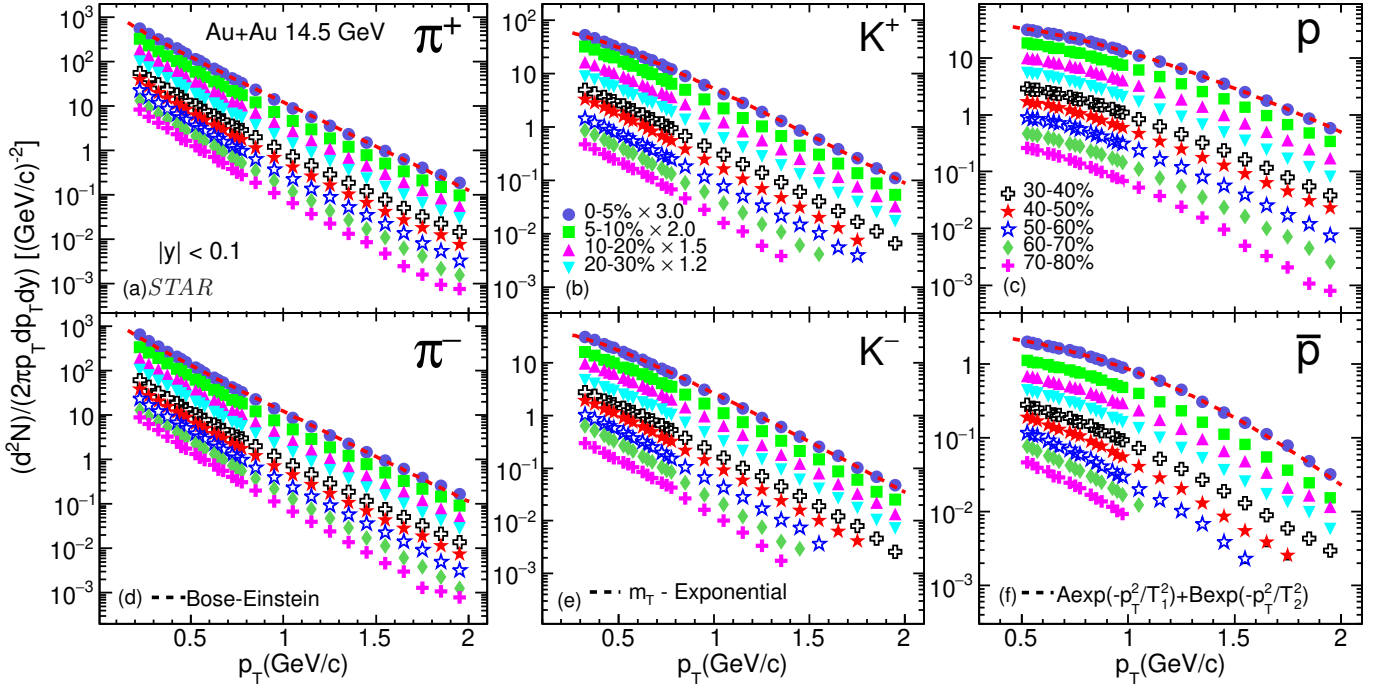
FIG. 7. The p_T spectra of $\pi^\pm$, $K^\pm$, p ($\bar{p}$) measured at midrapidity ($|y| < 0.1$) in Au+Au collisions at $\sqrt{s_{NN}} = 14.5$ GeV. Spectra are plotted for nine centrality classes, with some spectra multiplied by a scale factor to improve clarity, as indicated in the legend. The data points shown for $p_T = 0.4$–2.0 GeV/c for pions and kaons, and for 0.5–2.0 GeV/c for protons, are obtained using both TPC and TOF. Data points measured using only the TPC are shown for p_T in the range 0.2–0.8, 0.3–0.8 and 0.5–1.0 GeV/c for pions, kaons and protons, respectively. The p_T range 0.4–0.8 GeV/c, 0.4–0.8 GeV/c and 0.5–1.0 GeV/c for pions, kaons and protons, respectively, is the overlap region containing data measurements in both categories, namely, TPC only, and TPC+TOF. The p_T-spectra are fitted with a Bose-Einstein function for pions, an m_T-exponential for kaons, and a double exponential for (anti)protons. Statistical and systematic uncertainties are added in quadrature.

In the case of v_2 measurements, the η-gap is varied between 0.05 and 0.075. In total, about 100 combinations of such cut variations are considered and the RMS of the variation is taken as the systematic uncertainty. A maximum of 2% relative systematic uncertainty due to event cuts, and 1% due to track cuts, is found for the various centrality classes and for the various p_T and η bins.

V. RESULTS AND DISCUSSIONS

A. Transverse Momentum Spectra

The transverse momentum spectra for π^+, π^-, K^+, K^-, p, and $\bar{p}$ in Au+Au collisions at $\sqrt{s_{NN}} = 14.5$ GeV are presented in Fig. 7. The spectra are plotted for nine collision centralities 0–5%, 5–10%, 10–20%, 20–30%, 30–40%, 40–50%, 50–60%, 60–70%, 70–80%. Further information can be extracted from the particle p_T spectra through functional fitting in terms of dN/dy and $\langle p_T \rangle$. As mentioned earlier the functions used for this purpose are Bose-Einstein, m_T-exponential and double exponential for pions, kaons and protons, respectively. It can be inferred that the invariant yields exhibit a p_T dependence (decrease with increasing p_T) as well as a centrality dependence (decrease towards the peripheral collisions). The shapes of the kaon and (anti)proton spectra show a gradual flattening from peripheral to central collisions. The trend is less pronounced for pions. This flattening reflects a stronger effect of radial flow on particles with higher mass and for events with increasing centrality.

B. Average Transverse Momenta

Average transverse momenta quantitatively reflect the slopes of the measured p_T spectra of the particles. i.e., the transverse dynamics influences $\langle p_T \rangle$. The dependence of $\langle p_T \rangle$ on the number of nucleon participants $\langle N_{\text{part}} \rangle$ is shown in Fig. 8 for Au+Au collisions at $\sqrt{s_{NN}} = 14.5$ GeV. These averages are compared with the corresponding results from Au+Au collisions at $\sqrt{s_{NN}} = 7.7$, 11.5, 19.6, 27, 39, 62.4, and 200 GeV measured by STAR in earlier runs [8–11, 32, 60, 65]. It is seen from the figure that $\langle p_T \rangle$ of $\pi^\pm$, $K^\pm$ and $p(\bar{p})$ increases with increasing $\langle N_{\text{part}} \rangle$. This indicates an increase of radial flow from peripheral to central collisions [67]. Mean p_T and inferred radial flow also increase from pions to kaons, and from kaons to protons. The behavior of $\langle p_T \rangle$ as a function of
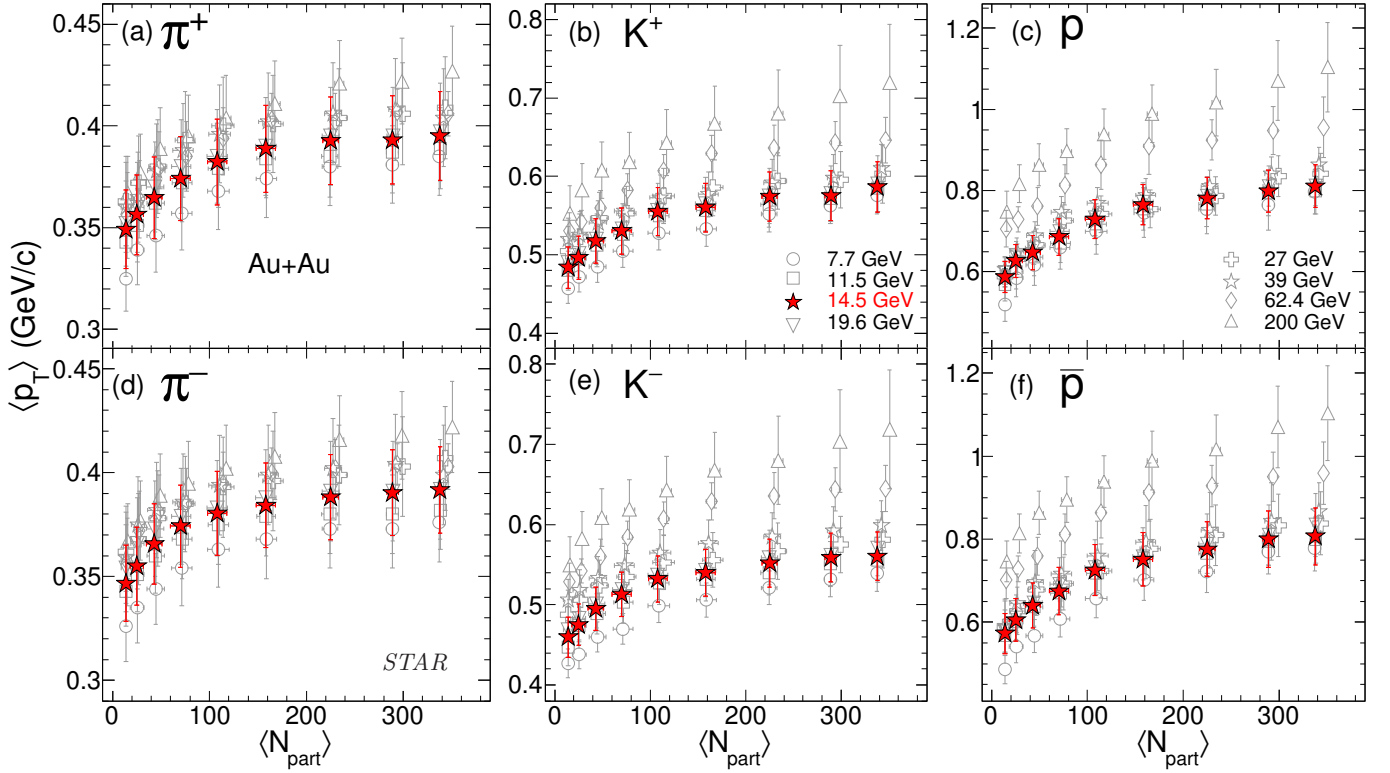
FIG. 8. $\langle p_T \rangle$ of π^+, K^+ and $p(\bar{p})$ as a function of $\langle N_{\text{part}} \rangle$ for Au+Au collisions at $\sqrt{s_{\text{NN}}} = 14.5$ GeV. These averages are compared with the corresponding results from Au+Au collisions at $\sqrt{s_{\text{NN}}} = 7.7$, 11.5, 19.6, 27, 39, 62.4, and 200 GeV measured by STAR in earlier runs [32, 60, 65]. Statistical and systematic uncertainties have been added in quadrature.

$\langle N_{\text{part}} \rangle$ in Au+Au collisions at $\sqrt{s_{\text{NN}}} = 14.5$ GeV is similar within error bars to what is observed at other BES-I energies, although it slowly increases with collision energy. The values of $\langle p_T \rangle$ for π^+, π^-, K^+, K^-, p, and $\bar{p}$ are listed in Table V for Au+Au collisions at $\sqrt{s_{\text{NN}}} = 14.5$ GeV.

C. Particle Yields

The particle production in a collision centrality interval is defined as dN/dy or particle yield, which we measure at midrapidity ($|y| < 0.1$) and is obtained by integrating over p_T. The measured dN/dy is shown in Fig. 9 for π^+, π^-, K^+, K^-, p and $\bar{p}$, normalized with $0.5 \times \langle N_{\text{part}} \rangle$, as a function of $\langle N_{\text{part}} \rangle$ in Au+Au collisions at $\sqrt{s_{\text{NN}}} = 14.5$ GeV. These yields are compared with the corresponding resul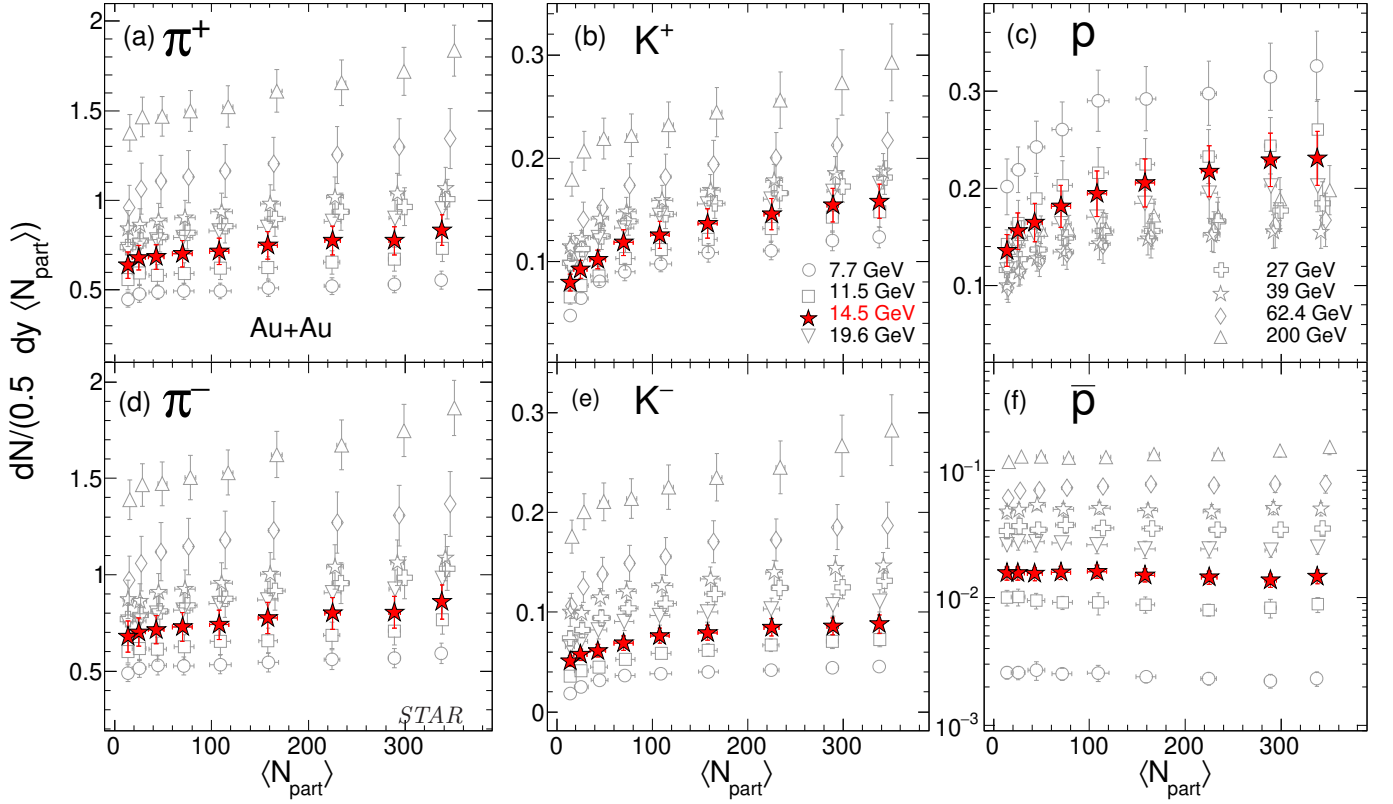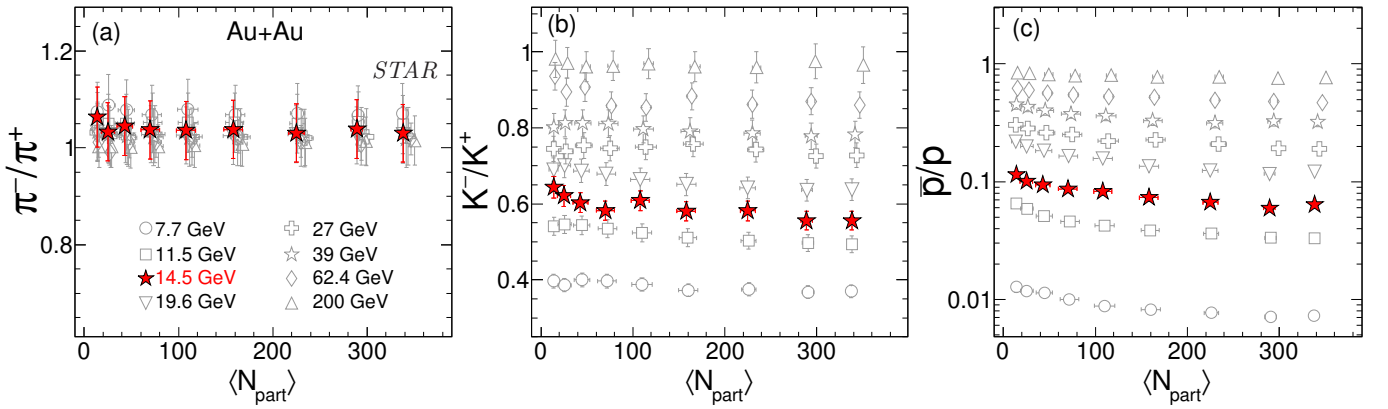ts from Au+Au collisions at $\sqrt{s_{\text{NN}}} = 7.7$, 11.5, 19.6, 27, 39, 62.4, and 200 GeV measured by STAR in earlier runs [8–11, 32, 60, 65]. The values of dN/dy for π^+, π^-, K^+, K^-, p, and $\bar{p}$ are also tabulated in Table IV for Au+Au collisions at $\sqrt{s_{\text{NN}}} = 14.5$ GeV.

The pion, kaon, and proton yields slowly increase from peripheral to central collisions. This may indicate contributions from hard processes which depend on the number of nucleon-nucleon binary collisions, increasing with

N_{part} more than linearly [68]. The antiproton yields remain almost flat with centrality. This may be due to an increasing baryon-antibaryon annihilation effect with increasing centrality. The yields of pions, kaons, and antiprotons all increase with increasing collision energy. However, the yield of protons shows the opposite trend and decreases up to 39 GeV after which it starts to increase. This reflects an increase in baryon density due to baryon stopping at lower energies [28, 32, 69]. The results in Au+Au collisions at $\sqrt{s_{\text{NN}}} = 14.5$ GeV show a similar behaviour as observed by STAR at other energies [8–11, 32, 60, 65].

D. Particle Ratios

Particle ratios provide additional information about particle production and the system evolution in high-energy heavy-ion collisions. In this context, we have analyzed particle ratios in Au+Au collisions at $\sqrt{s_{\text{NN}}} = 14.5$ GeV, and compared to published results for Au+Au collisions at other collision energies [8–11, 32, 60, 65].

Figure 10 shows the dependence of the antiparticle to particle ratios on $\langle N_{\text{part}} \rangle$ in Au+Au collisions at $\sqrt{s_{\text{NN}}} = 14.5$ GeV. These ratios are compared with the corresponding results from Au+Au collisions at $\sqrt{s_{\text{NN}}} = 7.7$,

FIG. 9. dN/dy of π^+, π^-, K^+, K^-, p and $\bar{p}$ scaled by $(0.5 \times \langle N_{\mathrm{part}}\rangle)$ as a function of $\langle N_{\mathrm{part}}\rangle$ for Au+Au collisions at $\sqrt{s_{NN}}=$ 14.5 GeV. These yields are compared with the corresponding results from Au+Au collisions at $\sqrt{s_{NN}} = 7.7$, 11.5, 19.6, 27, 39, 62.4, and 200 GeV measured by STAR in earlier runs [32, 60, 65]. Statistical and systematic uncertainties have been added in quadrature.

FIG. 10. π^-/π^+, K^-/K^+ and $\bar{p}/p$ ratios as a function of $\langle N_{\mathrm{part}}\rangle$ in Au+Au collisions at $\sqrt{s_{NN}} = 14.5$ GeV. These ratios are compared with the corresponding results from Au+Au collisions at $\sqrt{s_{NN}} = 7.7$, 11.5, 19.6, 27, 39, 62.4, and 200 GeV measured by STAR in earlier runs [32, 60, 65]. Statistical and systematic uncertainties have been added in quadrature.

11.5, 19.6, 27, 39, 62.4, and 200 GeV measured by STAR in earlier runs [8–11, 32, 60, 65]. The π^-/π^+ ratio has no significant centrality dependence and hovers around unity for all energies. At lower energies, including Au+Au collisions at $\sqrt{s_{NN}} = 14.5$ GeV, this ratio is slightly greater than one, which is due to isospin conservation and the contribution from decays of resonances like Δ baryons [28, 32]. This effect is more visible at lower energies due to the comparatively smaller yield of pions. The K^-/K^+ ratio is almost flat within uncertainties across all centralities. However, this K^-/K^+ ratio shows an increase with increasing beam energy. This is because at lower energies, associated production is the dominant mechanism, producing only K^+, whereas with
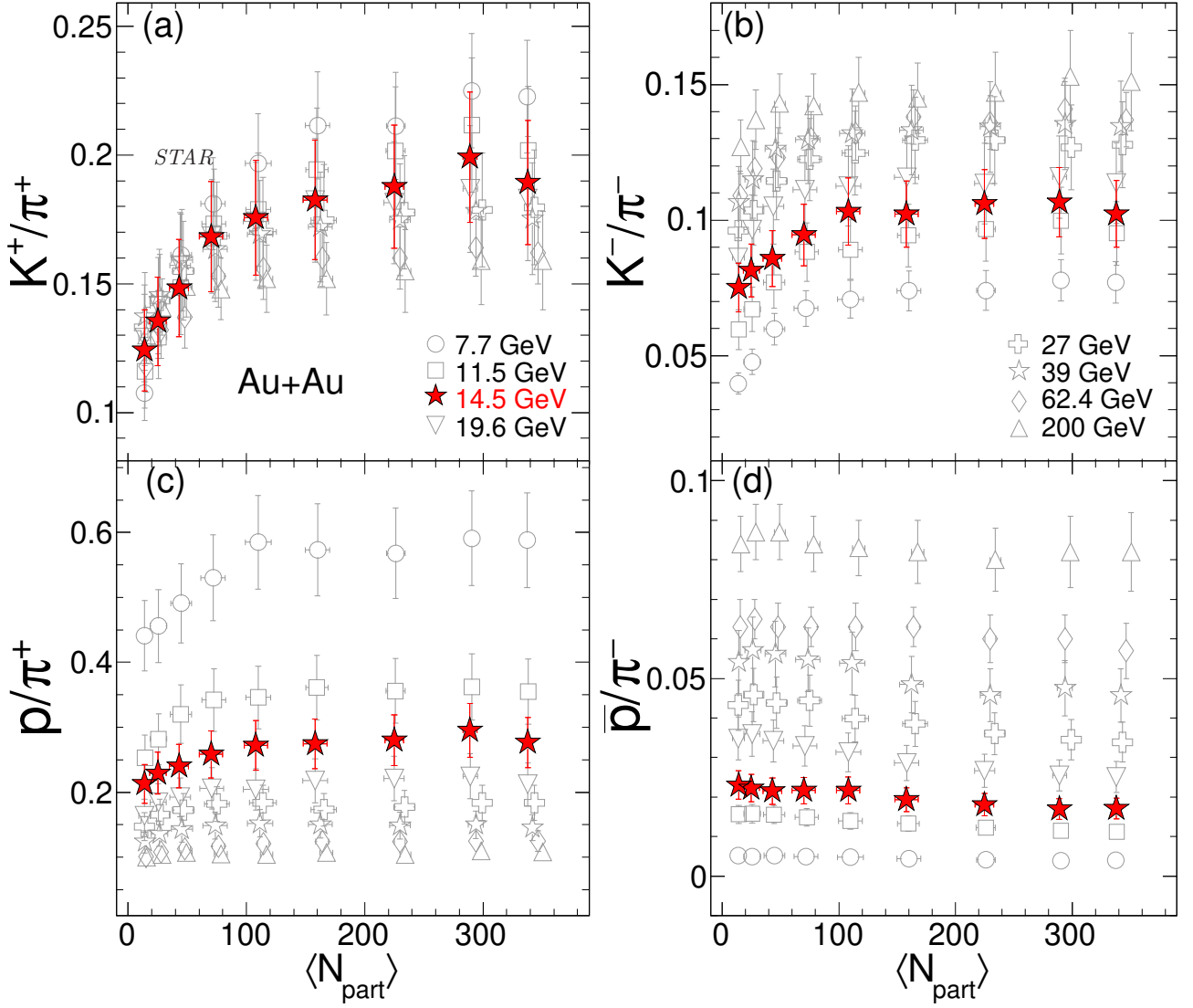
FIG. 11. K^+/π^+, K^-/π^-, p/π^+ and $\bar{p}/\pi^-$ ratios as a function of $\langle N_{\text{part}} \rangle$ in Au+Au collisions at $\sqrt{s_{\text{NN}}} = 14.5$ GeV. These ratios are compared with the corresponding results from Au+Au collisions at $\sqrt{s_{\text{NN}}} = 7.7, 11.5, 19.6, 27, 39, 62.4,$ and 200 GeV measured by STAR in earlier runs [32, 60, 65]. Statistical and systematic uncertainties have been added in quadrature.

increasing energy, pair production dominates, producing both K^+ and K^- [28, 32]. The $\bar{p}/p$ ratio shows a modest increase from central to peripheral collisions, which could be attributed to an increase in proton yields as a result of baryon stopping and/or a decrease in antiproton yields due to annihilation in central collisions [28, 32]. This ratio also increases with increasing collision energy. All these antiparticle-to-particle ratios in Au+Au collisions at $\sqrt{s_{\text{NN}}} = 14.5$ GeV follow the same general patterns as observed at other energies [8–11, 32, 60, 65].

Various ratios of different particle species such as K^+/π^+, K^-/π^-, p/π^+ and $\bar{p}/\pi^-$ are shown in Fig. 11 for Au+Au collisions at $\sqrt{s_{\text{NN}}} = 14.5$ GeV. Previously published results from the STAR experiment at other beam energies [8–11, 32, 60, 65] are also shown for comparison. Both K^+/π^+ and K^-/π^- ratios increase from

peripheral to mid-central collisions and then remain almost independent of $\langle N_{\text{part}} \rangle$. This pattern is due to strangeness equilibrium described in various thermodynamical models [70, 71] and is also impacted by baryon stopping at midrapidity. The results from Au+Au collisions at $\sqrt{s_{\text{NN}}} = 14.5$ GeV fit well in the energy dependence trend. The p/π^+ ratio increases slowly from peripheral to central collisions, whereas the $\bar{p}/\pi^-$ ratio stays flat across all values of $\langle N_{\text{part}} \rangle$. Also, there is a decrease in the p/π^+ ratio and an increase of the $\bar{p}/\pi^-$ ratio with increasing collision energy, which together can be attributed to baryon stopping at lower energies being prominent for central collisions.

E.   Kinetic Freeze-out Properties

The invariant yields and p_T spectra of particles give us tools to study the freeze-out properties of the system. There are two freeze-out stages observed in high-energy heavy-ion collision experiments: chemical freeze-out and kinetic freeze-out. First, inelastic collisions among the particles cease, defining the chemical freeze-out stage. After that point, there is no further production of new particles, and the yields of particle types becomes fixed. Various thermodynamic models are widely applied to extract the information of this stage in terms of chemical freeze-out temperature and baryon chemical potential [4, 32, 72, 73]. Thereafter, the particles collide only elastically. After further expansion of the system, as the inter-particle separation becomes large, such elastic collisions between particles also cease, leading to the kinetic freeze-out stage. The momenta of the particles are fixed after this point, and the particles freely propagate to the detector. The particle p_T spectra thus contain information about the kinetic freeze-out stage. Hydrodynamics inspired models such as the Blast-Wave model are used to extract the kinetic freeze-out properties [4, 32, 60, 66]. This stage is characterized by the kinetic freeze-out temperature T_k and radial flow velocity β, which carry signatures of the transverse expansion of the system. Here, we follow the previously adopted procedures to study the kinetic freeze-out properties in Au+Au collisions at $\sqrt{s_{NN}} = 14.5$ GeV. The chemical freeze-out properties are not discussed in this paper as the final measurements for strange hadrons yields for Λ and Ξ are not available. These will be reported in a future STAR paper.

The calculation of kinetic freeze-out parameters is carried out through a Blast-Wave model [66] fit to the measured particle p_T spectra in Au+Au collisions at $\sqrt{s_{NN}} = 14.5$ GeV. It is a hydrodynamics inspired model in which the particles are assumed to be locally thermalized at the kinetic freeze-out temperature T_k and move with a common radial flow velocity profile β. For such a radially boosted uniform hard sphere, the transverse momentum distribution of the produced particles can be written as [32, 60, 66]

$$\frac{dN}{p_T dp_T} \propto \int_0^R r dr \, m_T I_0 \left(\frac{p_T \sinh \rho(r)}{T_k} \right) \times K_1 \left(\frac{m_T \cosh \rho(r)}{T_k} \right), \quad (11)$$

where $m_T = \sqrt{p_T^2 + m^2}$ is the transverse mass of the particle, $\rho(r) = \tanh^{-1} \beta$, and I_0 and K_1 are modified Bessel functions. A flow velocity profile of the following form is used [32, 60, 66].

$$\beta = \beta_s (r/R)^n, \quad (12)$$

where β_S is the surface velocity, r/R is the radial position in the thermal source with radius R, and the exponent n in the flow velocity profile is a parameter. The average transverse radial flow velocity $\langle \beta \rangle$ is given by $\langle \beta \rangle = \frac{2}{2+n} \beta_S$.
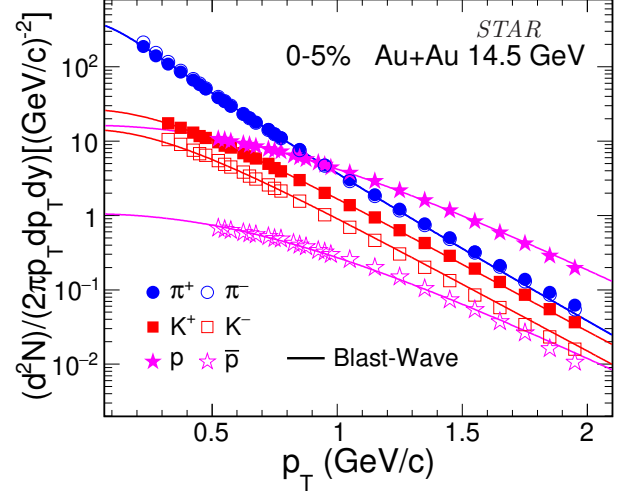

FIG. 12. Simultaneous Blast-Wave model fits to the p_T-spectra of $\pi^\pm$, $K^\pm$, $p(\bar{p})$ from 0–5% central Au+Au collisions at $\sqrt{s_{NN}} = 14.5$ GeV. Uncertainties on experimental data represent statistical and systematic uncertainties added in quadrature, mostly smaller than the symbol size.

To extract the kinetic freeze-out parameters, simultaneous Blast-Wave model fits to the $\pi^\pm$, $K^\pm$ and $p(\bar{p})$ spectra are performed [32, 60, 66] as plotted in Fig. 12 for central Au+Au collisions at $\sqrt{s_{NN}} = 14.5$ GeV. The low-p_T region of the pion spectra is affected by resonance decays, and therefore the pion spectra above $p_T > 0.5$ GeV/c are used for fitting. The Blast-Wave model is not very suitable for fitting the high p_T region of the p_T spectra [74]. Hence, the Blast-Wave model fits are very sensitive to the p_T range used [75]. The previously optimized p_T ranges [32, 60, 75] are used for Au+Au collisions at $\sqrt{s_{NN}} = 14.5$ GeV to extract the kinetic freeze-out parameters. The fit ranges used for pions, kaons, and protons are 0.5–1.35 GeV/c, 0.3–1.35 GeV/c, and 0.5–1.25 GeV/c, respectively.

Figure 13 presents the kinetic freeze-out parameters T_k (Fig. 13(a)) and $\langle \beta \rangle$ (Fig. 13(b)) as a function of N_{part}, and presents the correlation between T_k and β (right) for Au+Au collisions at $\sqrt{s_{NN}} = 14.5$ GeV. These results are compared with published data for Au+Au collisions at $\sqrt{s_{NN}} = 7.7, 11.5, 19.6, 27, 39, 62.4,$ and 200 GeV measured by STAR in earlier runs [32, 60]. T_k shows a dependence on N_{part}, decreasing from peripheral to central collisions. This observation supports the prediction of a short-lived fireball in the case of peripheral collisions [76]. The average flow velocity $\langle \beta \rangle$, on the other hand, increases from peripheral to central collisions. This indicates a higher rate of expansion of the system in central collisions. It is also seen that higher RHIC
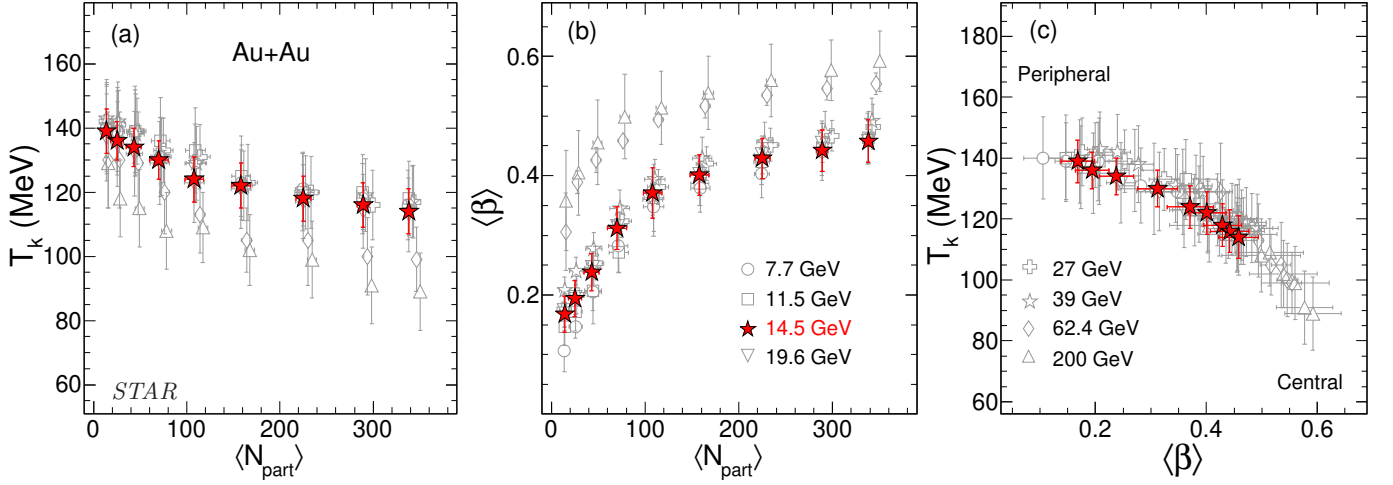
FIG. 13. Panel (a): T_k as a function of $\langle N_{\mathrm{part}} \rangle$. Panel (b): β as a function of $\langle N_{\mathrm{part}} \rangle$. Panel (c): variation of T_k with β. In all three panels, present results for Au+Au collisions at $\sqrt{s_{\mathrm{NN}}} = 14.5$ GeV are shown in comparison with the same quantities for Au+Au collisions at $\sqrt{s_{\mathrm{NN}}} = 7.7$, 11.5, 19.6, 27, 39, 62.4, and 200 GeV measured by STAR in earlier runs [32]. Systematic uncertainties are shown. Statistical uncertainties are much smaller than systematic ones.

energies such as 62.4 and 200 GeV, have comparatively higher β than other BES-I energies. Lastly, the correlation plot between T_k and β confirms an anti-correlation between these two quantities, i.e. as T_k decreases, β increases. The behavior of the kinetic freeze-out parameters in Au+Au collisions at $\sqrt{s_{\mathrm{NN}}} = 14.5$ GeV is consistent with previous observations [32, 60]. The extracted fit parameters T_k, $\langle \beta \rangle$, and n along with the χ^2/ndf values from the Blast-Wave model fits in Au+Au collisions at $\sqrt{s_{\mathrm{NN}}} = 14.5$ GeV are reported in Table VI.

F. Azimuthal Anisotropy

1. The event plane resolution

Due to the finite multiplicity in each event, the event plane angle (Ψ_n) deviates from the reaction plane azimuthal angle (Ψ_R). Hence a resolution correction needs to be performed to obtain the correct measurement of the flow coefficients (v_n) [54]. For this analysis, the event planes are determined from the TPC in the midrapidity region, and from the BBC at forward rapidity.

Figure 14 shows the second-order event-plane resolution from the TPC (panel (a)) and the first-order event-plane resolution from the BBC (panel (b)) as a function of centrality in Au+Au collisions at $\sqrt{s_{\mathrm{NN}}} = 14.5$ GeV. The event plane resolution has been calculated for nine collision centralities: 0–5%, 5–10%, 10–20%, 20–30%, 30–40%, 40–50%, 50–60%, 60–70% and 70–80%. As the event plane resolution depends on the number of particles used for event plane reconstruction, it shows

a tendency to increase from peripheral to central collisions. On the other hand, the event plane is calculated using the anisotropic flow of the event itself, and therefore it tends to decrease towards central collisions where flow values are small. Because of these two competing effects, the overall resolution first increases from peripheral to mid-central collisions and then decreases. Figure 14 includes event plane resolutions for the same methods at other BES-I energies studied previously by STAR. Due to limited statistics and poor BBC resolution, the FTPC [77] event plane is used instead of BBC at 39 GeV. As expected the resolution of the TPC and BBC event planes decreases as the collision energy increases, since the resolution depends on the multiplicity and on the v_2 signal [54]. The 14.5 GeV resolution does not lie between that observed at the adjacent beam energies above and below, and instead is slightly lower than a smooth trend would predict. This is a consequence of the additional material of the Heavy Flavor Tracker close to the beam pipe, which was present only during the 2014 run at 14.5 GeV. The event plane resolution corrections to the observed v_n are applied on an event-by-event basis [55, 56]. In this method, the resolution correction has been applied by dividing the flow coefficient of each track, $\cos n(\phi - \Psi_n)$, by the event-plane resolution $\langle R \rangle$ for the appropriate centrality class.

2. Comparison of v_2 from different methods

Figure 15 presents inclusive charged particle $v_2(p_{\mathrm{T}})$, using various methods, for Au+Au collisions at $\sqrt{s_{\mathrm{NN}}} = 14.5$ GeV. The methods have different sensitivities to nonflow effects and v_2 fluctuations. For the purpose
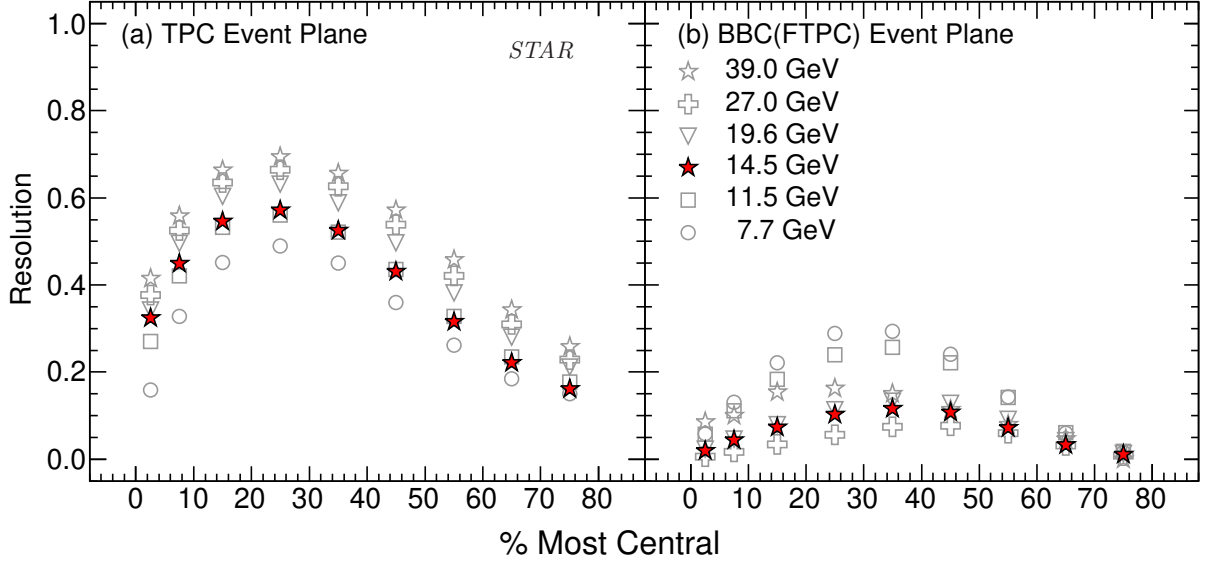
FIG. 14. The event plane resolution calculated for Au+Au collisions at $\sqrt{s_{NN}} = 14.5$ GeV (solid star) as a function of centrality. The current results are compared with those for 7.7, 11.5, 14.5, 19.6, 27 and 39 GeV. Panel (a) shows the second-order event plane resolution reconstructed by using the TPC tracks ($|\eta| < 1$). Panel (b) shows the second-order event plane resolution for 39 GeV from the FTPC ($2.5 < |\eta| < 4.0$) and the first-order event plane resolution from the inner tiles of the BBC ($3.8 < |\eta| < 5.2$).
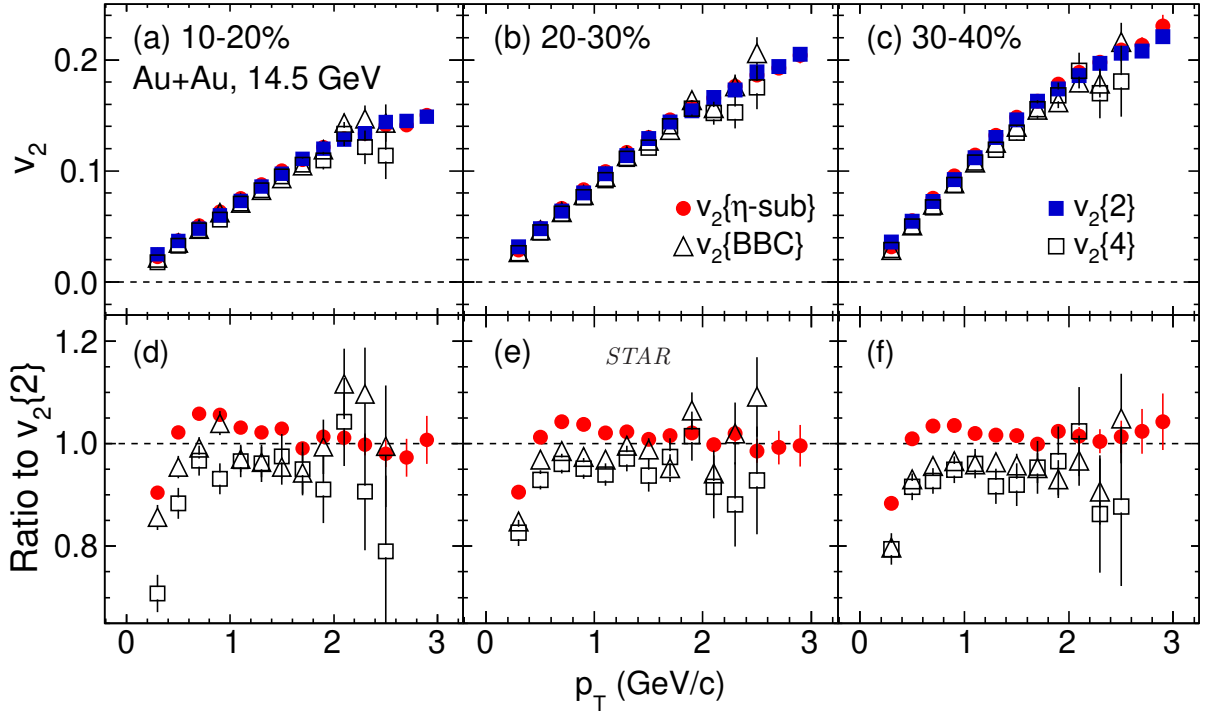
FIG. 15. Inclusive charged particle v_2 at mid-pseudorapidity ($|\eta| < 1.0$) as a function of p_T for (a) 10–20%, (b) 20–30% and (c) 30–40% centralities in Au + Au collisions at $\sqrt{s_{NN}} = 14.5$ GeV. Results are shown for the η-sub event plane method (circles), BBC event plane (open triangles), 2-particle (solid squares) and 4-particle (open squares) cumulants. The bottom panels (d), (e) and (f) show the ratio of v_2 measured using the various methods with respect to the 2-particle cumulant result, $v_2\{2\}$. Errors are statistical. Systematic uncertainties are small ($\sim 2\%$).
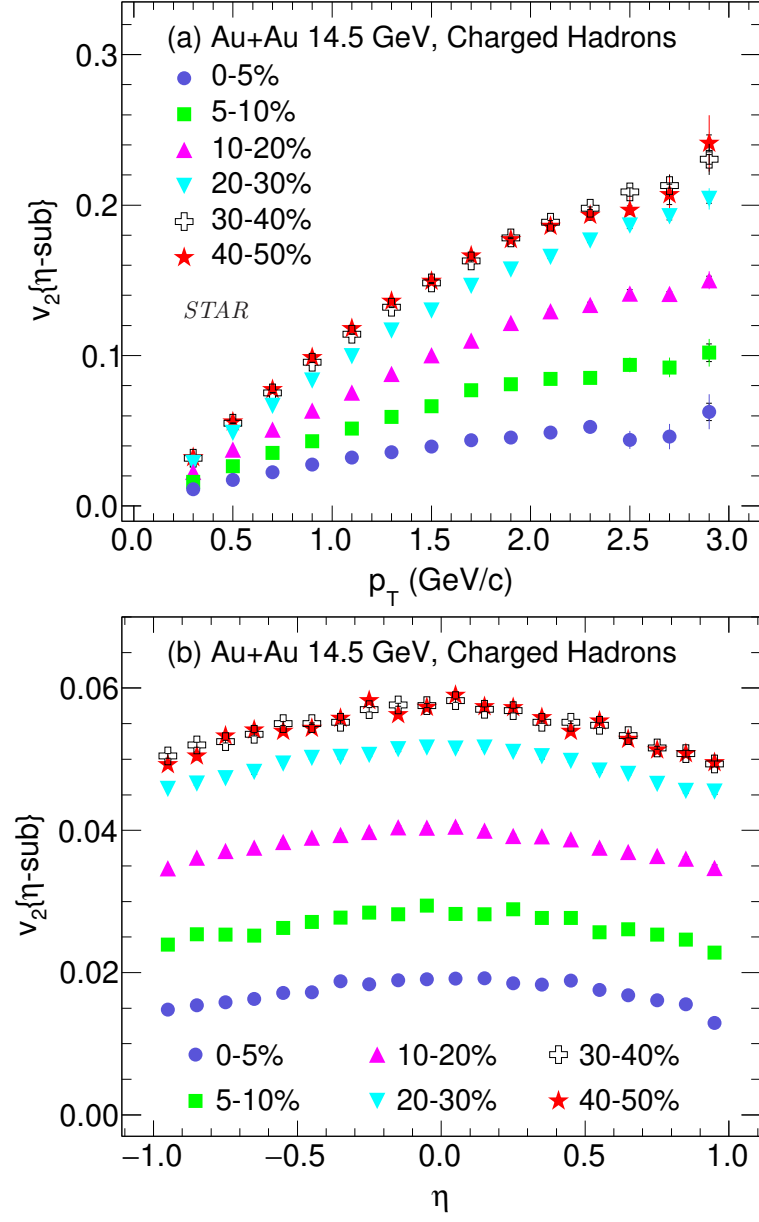
FIG. 16. Inclusive charged particle elliptic flow v_2 at mid-pseudorapidity ($|\eta| < 1.0$) as a function of transverse momentum p_T and the p_T-integrated $v_2(\eta)$ for six centrality classes, obtained using the η-sub event plane method in Au+Au collisions at $\sqrt{s_{NN}} = 14.5$ GeV. Statistical uncertainties are shown by error bars, while systematic uncertainties are smaller and are plotted as caps.

of exact comparisons, v_2 for each method is divided by the elliptic flow based on the two-particle cumulant method (denoted $v_2\{2\}$) and the ratios are shown in the lower panels of Fig. 15. The difference of $v_2\{2\}$ compared to $v_2\{BBC\}$, $v_2\{4\}$, and $v_2\{\eta-sub\}$ depends on the p_T range. A larger difference is observed in the low-p_T region ($p_T < 1$ GeV/c). From $p_T \sim 1$ GeV/c and above, the difference stays roughly constant. The difference between $v_2\{BBC\}$ and $v_2\{4\}$ is relatively small, and is less dependent on p_T. The results suggest that nonflow contributions to the event plane and two-particle correlation methods depend on p_T. They also indicate that the use of the first-order reaction plane (BBC event plane) to study the second harmonic flow reduces flow fluctuations which are not correlated between different harmonics.

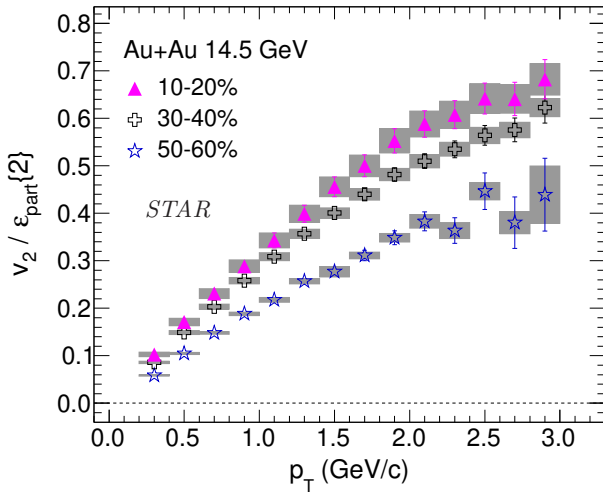### 3. Dependence of v_2 on transverse momentum, pseudorapidity and centrality

FIG. 17. The ratio $v_2/\epsilon_{part}\{2\}$ for inclusive charged particle elliptic flow v_2 at mid-pseudorapidity as a function of p_T for 10–20%, 30–40%, and 50–60% collision centralities in Au+Au collisions at $\sqrt{s_{NN}} = 14.5$ GeV. The v_2 data are from the η-sub event plane method, and the spatial eccentricity $\epsilon_{part}\{2\}$ is based on a Glauber calculation. The error bars and shaded boxes present the statistical and systematic uncertainties, respectively.

Results for charged particle v_2 as a function of p_T for six collision centrality intervals are presented in panel (a) of Fig. 16. The v_2 shows a monotonically increasing trend with increasing p_T for Au+Au collisions at $\sqrt{s_{NN}} = 14.5$ GeV. The differential v_2 also exhibits centrality dependence. The trends of $v_2(p_T)$ are similar to those observed at other BES-I energies. Panel (b) of Fig. 16 presents the p_T-integrated $v_2(\eta)$ for six centrality classes. The v_2 has a weak dependence on η. Also, there is a clear centrality dependence observed in v_2. The trend of $v_2(\eta)$ is similar

to that for other BES-I energies [8–11, 32, 60, 65].

The larger magnitude of v_2 in peripheral collisions can be attributed to the larger initial eccentricity in coordinate space for peripheral collisions. The participant eccentricity is the initial configuration space eccentricity of the participating nucleons. The root-mean-square participant eccentricity ($\epsilon_{part}\{2\}$) is calculated from a MC Glauber model [78, 79] and reported in Table II.

In Fig. 17, the centrality dependence of $v_2(p_T)$ over eccentricity $\epsilon_{part}\{2\}$ is shown for Au + Au collisions at $\sqrt{s_{NN}} = 14.5$ GeV for 10–20%, 30–40%, and 50–60% collision centralities. Central collisions have higher $v_2/\epsilon_{part}\{2\}$ than peripheral collisions. This finding is consistent with a picture where collective interactions are stronger in collisions with a larger number of participants. The centrality dependence of $v_2/\epsilon_{part}\{2\}$ is observed to be similar to that reported previously by STAR [8–11, 32, 60, 65].

4. Beam energy dependence of v_2

The BES-I data from the STAR experiment offer an opportunity to study the collision energy dependence of v_2 using a wide-acceptance detector at midrapidity. Figure 18 shows the comparison of the p_T dependence of $v_2\{4\}$ for $\sqrt{s_{NN}} = 14.5$ GeV at 10–20%, 20–30%, and 30–40% centralities with other published results from STAR [8–11, 32, 60, 65, 80, 81] and ALICE [82]. One reason to select the $v_2\{4\}$ results for this comparison is to keep the method for v_2 extraction consistent with the published results from ALICE. Another reason is that $v_2\{4\}$ is found to have low sensitivity to nonflow correlations. The 200 GeV data are empirically fit by a fifth-order polynomial function. For comparison, the v_2 from other energies are divided by the fit function and shown in the lower panels of Fig. 18. We choose the 200 GeV data as a reference because its statistical uncertainties are smallest. For p_T below 2 GeV/c, the v_2 values rise with increasing collision energy. Above $p_T \sim 2$ GeV/c, the v_2 values are comparable within statistical uncertainties. The increase of $v_2(p_T)$ as a function of energy can be attributed to the change of chemical composition from low to high energies [32] and/or larger collectivity at the higher collision energies.

Figure 19 presents the η dependence of $v_2\{\eta-sub\}$ for $\sqrt{s_{NN}} = 7.7$ to 200 GeV. The 14.5 GeV data points are plotted as solid red stars. The dashed red line in panel (a) in Fig. 19 shows an empirical fit to the results from Au+Au collisions at $\sqrt{s_{NN}} = 7.7$ GeV. Panel (b) presents the ratio of $v_2(\eta)$ from all beam energies with respect to this fitted curve. The $v_2(\eta)$ changes shape as the beam energy decreases. The $v_2(\eta)$ shape at 14.5 GeV follows the trend of other beam energies.
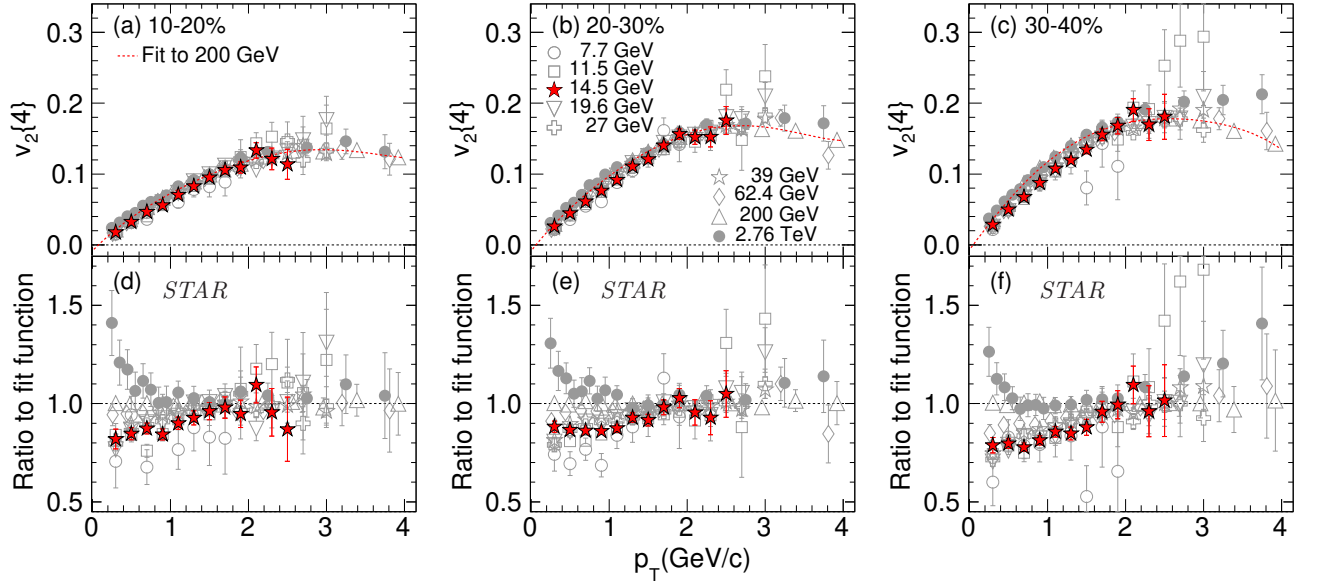
FIG. 18. The upper panels (a), (b) and (c) show inclusive charged particle elliptic flow $v_2\{4\}$ versus p_T for various collision energies ($\sqrt{s_{NN}}$ = 7.7 GeV to 2.76 TeV) at three centralities: 10–20%, 20–30%, and 30–40%. The present results at 14.5 GeV (and also for other energies except 2.76 TeV) are for mid-pseudorapidity ($|\eta| < 1.0$). The measurement of v_2 at 2.76 TeV was done at mid-pseudorapidity ($|\eta| < 0.8$). Furthermore, all results for $\sqrt{s_{NN}}$ = 7.7 to 200 GeV are for Au+Au collisions and those for 2.76 TeV are for Pb+Pb collisions. The dashed red curves show 5th-order polynomial function fits to the results from Au+Au collisions at $\sqrt{s_{NN}}$ = 200 GeV. The lower panels (d), (e) and (f) show the ratio of $v_2\{4\}$ versus p_T for all $\sqrt{s_{NN}}$ with respect to the fit curve. Error bars are shown only for statistical uncertainties. Systematic uncertainties are small ($\sim 2\%$)

5. Transverse momentum, pseudorapidity, and centrality dependence of v_1

Measurements of the charged particle $v_1(p_T)$ in three centralities (0-10%, 10–40% and 40-80%) in Au+Au collisions at $\sqrt{s_{NN}}$ = 7.7 – 39 GeV are presented in Fig. 20. This work focuses only on the (pseudo)rapidity-odd component of the first harmonic coefficient (directed flow). Since this component by definition has the property $v_1(-\eta, p_T) = -v_1(\eta, p_T)$, the integral of $v_1(\eta, p_T)$ over any symmetric η range is zero. Therefore, in presenting the above-mentioned pseudorapidity-integrated p_T dependence, the v_1 at negative η is multiplied by -1. By definition, $v_1(p_T)$ must approach zero as p_T approaches zero. The observed v_1 starts from a negative value, then crosses zero around $p_T \sim$ 1–2 GeV depending on collision energy and centrality. We see that, in more peripheral collisions and/or at higher energies, the sign change might occur at higher p_T compared to more central collisions and lower energies. The values of the charged particle $v_1(p_T)$ for three centralities (0-10%, 10–40% and 40-80%) in Au+Au Au+Au collisions at $\sqrt{s_{NN}}$ = 14.5 GeV are listed in Table VII.

Figure 21 presents the charged particle v_1 as a function of η for three centrality classes in Au+Au collisions at $\sqrt{s_{NN}}$ = 7.7 – 39 GeV. The v_1 slope at midrapidity for charged particles increases from central to peripheral collisions. The trend in $v_1(p_T, \eta)$ as a function of centrality for $\sqrt{s_{NN}}$ = 7.7 – 39 GeV shows a similar behavior as

observed in other STAR published data [8–11, 32, 60, 65]. The values of the charged particle v_1 as a function of η for three centrality classes in Au+Au Au+Au collisions at $\sqrt{s_{NN}}$ = 14.5 GeV are listed in Table VIII.

6. Beam-energy dependence of v_1

Panel (a) in Fig. 22 shows a comparison of $v_1(\eta)$ at 30–60% centrality for Au+Au collisions at $\sqrt{s_{NN}}$ = 7.7 – 200 GeV and for Pb+Pb collisions at $\sqrt{s_{NN}}$ =2.76 TeV. We observe a clear energy dependence in the $v_1(\eta)$ for $\sqrt{s_{NN}}$ = 7.7 GeV - 2.76 TeV. To calculate the slope of v_1, we fit the data with a function $F1 \times y + F3 \times y^3$. The linear term in this function ($F1$) gives the v_1 slope (dv_1/dy). Panel (b) in Fig. 22 shows the beam energy dependence of dv_1/dy for 0-10%, 10–40% and 40-80% centralities for Au+Au collisions at $\sqrt{s_{NN}}$ = 7.7 – 200 GeV. The dv_1/dy for 30-60% centrality for the above energies are compared with the same from the published data from Au+Au collisions at $\sqrt{s_{NN}}$ = 200 GeV at RHIC and Pb+Pb collisions at $\sqrt{s_{NN}}$ = 2.76 TeV at the LHC. We observe a smooth increase in the magnitude of dv_1/dy at mid-pseudorapidity with decreasing beam energy for 30-60% centrality.
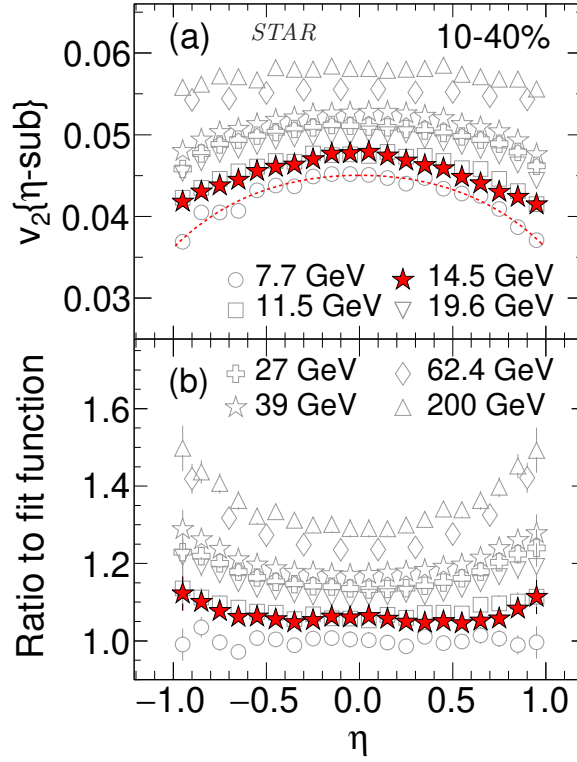
FIG. 19. Panel (a) shows inclusive charged particle elliptic flow $v_2(\eta\text{-sub})$ versus η at mid-pseudorapidity for various collision energies ($\sqrt{s_{\mathrm{NN}}} = 7.7$ GeV to 200 GeV). The dashed red curve shows an empirical fit to the result from Au+Au collisions at $\sqrt{s_{\mathrm{NN}}} = 7.7$ GeV. Panel (b) shows the ratio of $v_2\{4\}$ versus η for all $\sqrt{s_{\mathrm{NN}}}$ with respect to the fit curve. The results are shown for 10–40% collision centrality. Error bars are shown only for statistical uncertainties.

G.   Model Comparisons

Measurements from STAR suggest that at 7.7 GeV and 11.5 GeV, particle production is dominated by hadronic processes, whereas at energies around 20 GeV and above, partonic degrees of freedom become more important [38–42]. The $\sqrt{s_{\mathrm{NN}}} = 14.5$ GeV Au+Au collisions analyzed here thus lie in a transition region of great interest. Various bulk properties of the system like $\langle p_{\mathrm{T}} \rangle$, dN/dy, particle ratios, elliptic flow v_2, and directed flow v_1 measured in Au+Au collisions at $\sqrt{s_{\mathrm{NN}}} = 14.5$ GeV are compared with calculations from AMPT (version 2.25t7d) [34] and UrQMD (version 3.3p1) [33]. The initial parameter settings for the models follow the recommendations in the cited papers. The UrQMD model treats only hadronic interactions whereas AMPT has two versions — a string melting version (denoted AMPT-SM) which allows for both partonic and hadronic interactions among the particles, while the default version of AMPT treats only hadronic interactions. Recently, there have been studies with the AMPT-SM model to explain the particle multiplicity and flow measurements at RHIC and LHC using different values of the parton cascade scattering cross-section such as 1.5 mb and 10 mb. It was found that a 1.5 mb scattering cross-section gives a better description of data at these energies [83, 84]. We have generated

AMPT-SM events with two different partonic cross sections (1.5 mb and 10 mb), denoted as AMPT 1.5mb and AMPT 10mb. The larger the partonic cross section, the later the hadronic cascade begins.

1.   Mean transverse momentum

The average p_{T} of π^+, K^+ and p as a function of $\langle N_{\mathrm{part}} \rangle$ obtained from UrQMD, AMPT 1.5mb and AMPT 10mb model calculations are compared with STAR measurements for Au+Au collisions at $\sqrt{s_{\mathrm{NN}}} = 14.5$ GeV in Fig. 23. The value of $\langle p_{\mathrm{T}} \rangle$ for all the studied particles is found to be too low in all AMPT-SM calculations. UrQMD is generally too low in $\langle p_{\mathrm{T}} \rangle$ also, but is closer to the data, and shows good agreement for protons.

2.   Particle yields

Figure 24 shows dN/dy divided by $0.5 \times \langle N_{\mathrm{part}} \rangle$ versus $\langle N_{\mathrm{part}} \rangle$ for π^+, K^+ and p from Au+Au collisions at $\sqrt{s_{\mathrm{NN}}} = 14.5$ GeV. The STAR measurements are compared with UrQMD and with AMPT 1.5mb and AMPT
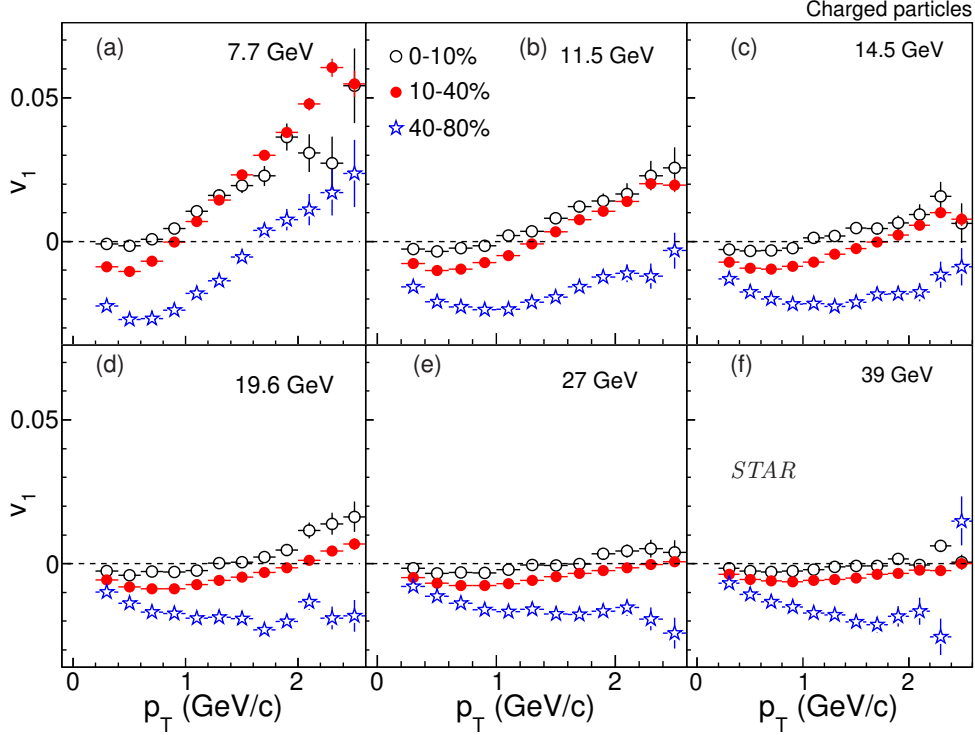
Charged particles

FIG. 20. Charged particle v_1 as a function of p_T in Au+Au collisions at $\sqrt{s_{NN}} = 7.7 - 39$ GeV for 0–10%, 10–40% and 40–80% centrality intervals. Error bars are shown only for statistical uncertainties. Systematic uncertainties are small ($\sim 2\%$).

10mb. UrQMD and AMPT are close to the π^+ data for central collisions, but deviate for peripheral collisions. All models disagree markedly with K^+ measurements. In the case of protons, AMPT-SM is close, with AMPT 1.5mb being slightly but consistently closer, while UrQMD lies well below the data at all centralities.

3. Particle ratios

Antiparticle to particle ratios (π^-/π^+, K^-/K^+ and $\bar{p}/p$) as a function of $\langle N_{part} \rangle$ in Au+Au collisions at $\sqrt{s_{NN}} = 14.5$ GeV are shown in Fig. 25. These measured ratios are compared with UrQMD and AMPT-SM calculations. The pion ratios from all models are in close agreement with experiment, while AMPT gets the wrong trends for the kaons. The proton ratios from AMPT-SM are in good agreement with experiment, while UrQMD shows poor agreement.

Figure 26 shows STAR measurements of K^+/π^+, K^-/π^-, p/π^+ and $\bar{p}/\pi^-$ ratios as a function of $\langle N_{part} \rangle$ in Au+Au collisions at $\sqrt{s_{NN}} = 14.5$ GeV, along with UrQMD and AMPT-SM model calculations. K^+/π^+ and K^-/π^- ratios are under-predicted by all model calculations. In the case of p/π^+, AMPT-SM straddles the data, and in the case of $\bar{p}/\pi^-$, AMPT-SM shows good agreement. On the other hand, the latter two ratios are

not tracked by UrQMD.

4. Elliptic flow

Panels (a), (b) and (c) of Fig. 27 present the p_T dependence of $v_2\{\eta-\text{sub}\}$ for 14.5 GeV Au+Au collisions at 10–20%, 20–30% and 30–40% centralities. The STAR measurements are compared with UrQMD, AMPT 1.5mb, and AMPT 10mb. Panels (d), (e) and (f) of Fig. 27 present the ratio of the experimental data to each model calculation. The AMPT 1.5mb calculation exhibits the best agreement, with AMPT 10mb being consistently too high and UrQMD consistently too low. Figure 28 presents very similar comparisons as Fig. 27, except transverse momentum dependence is replaced by pseudorapidity dependence. Here, again we observe similar behavior, i.e. the AMPT 1.5mb calculation exhibits the better agreement.

5. Directed flow

Figure 29 presents charged particle $v_1(p_T)$ (panel (a)) and $v_1(\eta)$ (panel (b)) for 10–40% centrality Au+Au col-
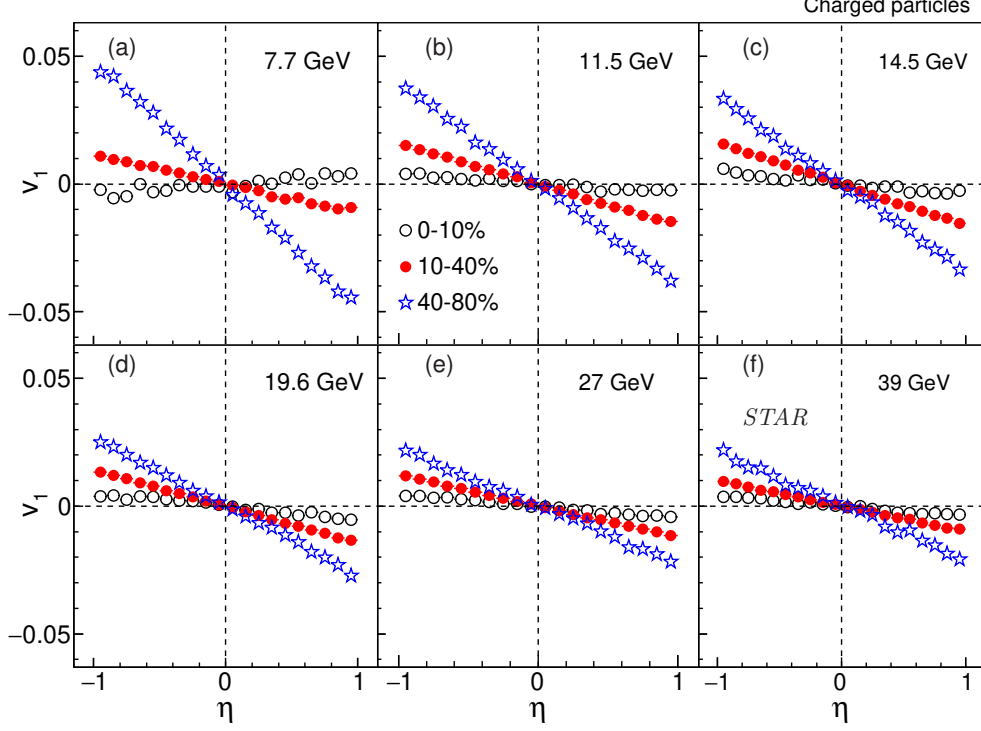
Charged particles

FIG. 21. Charged particle v_1 as a function of η in Au+Au collisions at $\sqrt{s_{NN}} = 7.7 - 39$ GeV for 0–10%, 10–40% and 40–80% centrality intervals. Error bars are shown only for statistical uncertainties. Systematic uncertainties are small ($\sim 2\%$).
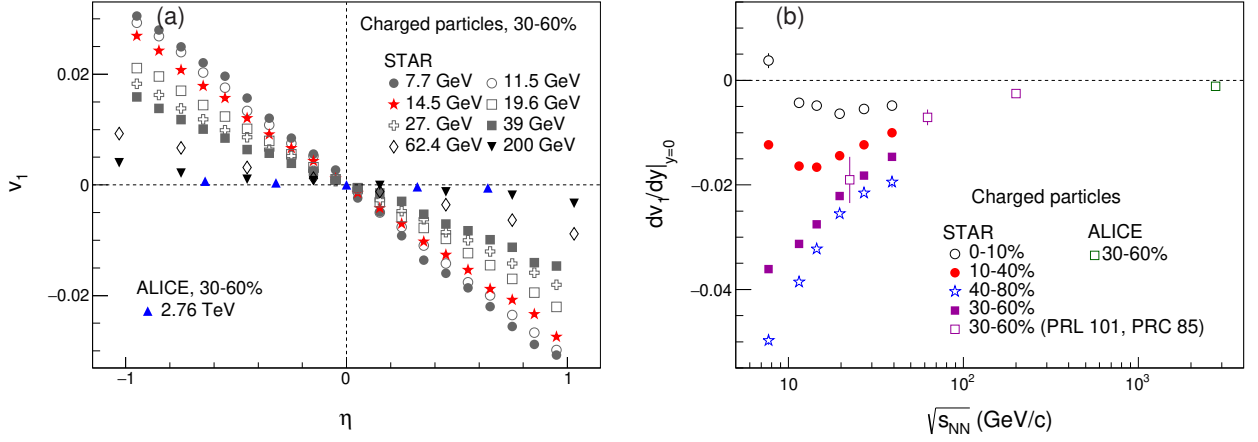

FIG. 22. Panel (a): Charged particle v_1 as a function of η in Au+Au collisions at $\sqrt{s_{NN}} = 7.7$–39 GeV for 30–60% centrality interval. Results are compared to 62.4 and 200 GeV Au+Au collisions at RHIC and to 2.76 TeV Pb+Pb collisions at the LHC. Panel (b): Charged particle v_1 slope, dv_1/dy, at mid-pseudorapidity as a function of $\sqrt{s_{NN}}$ for different centralities. Error bars are shown only for statistical uncertainties. Systematic uncertainties are small ($\sim 2\%$).

lisions at $\sqrt{s_{NN}} = 14.5$ GeV. These STAR measurements are compared to UrQMD, AMPT, AMPT 1.5mb, and AMPT 10mb model calculations.

UrQMD shows poor agreement with the v_1 measurements, whereas the default AMPT roughly tracks $v_1(p_T)$ up to $p_T \sim 1.8$ GeV/c. AMPT 1.5mb and AMPT 10mb

are both significantly worse than the default AMPT for $v_1(p_T)$. No model calculation agrees with the measured data for $v_1(\eta)$. The latest state-of-the-art models do not show even qualitative agreement with v_1 measurements for identified particles at BES-I energies [85]. It should be noted that in both AMPT-SM options, antibaryons
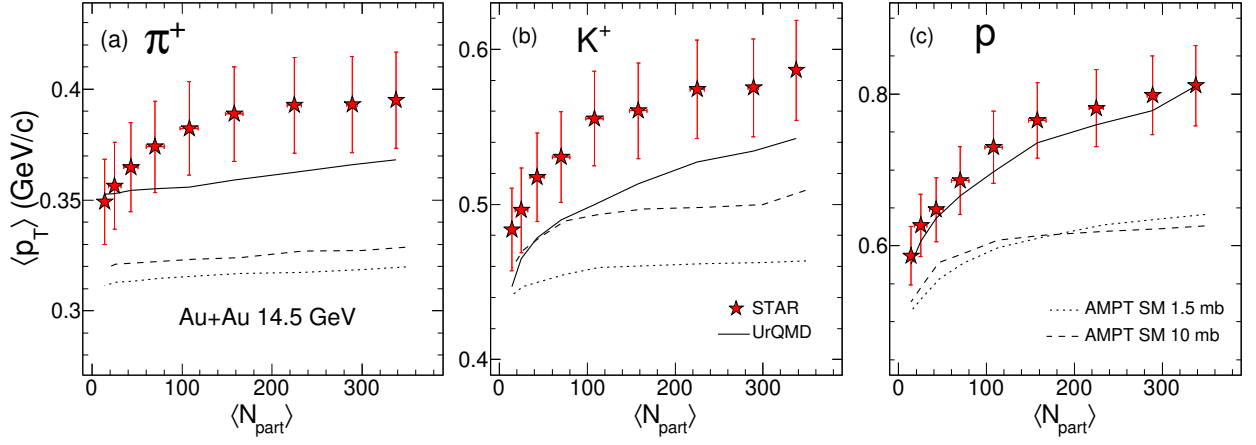
FIG. 23. $\langle p_T \rangle$ of π^+, K^+ and p as a function of $\langle N_{part} \rangle$ for Au+Au collisions at $\sqrt{s_{NN}} = 14.5$ GeV in STAR. These measurements are compared with UrQMD, AMPT 1.5mb and AMPT 10mb.
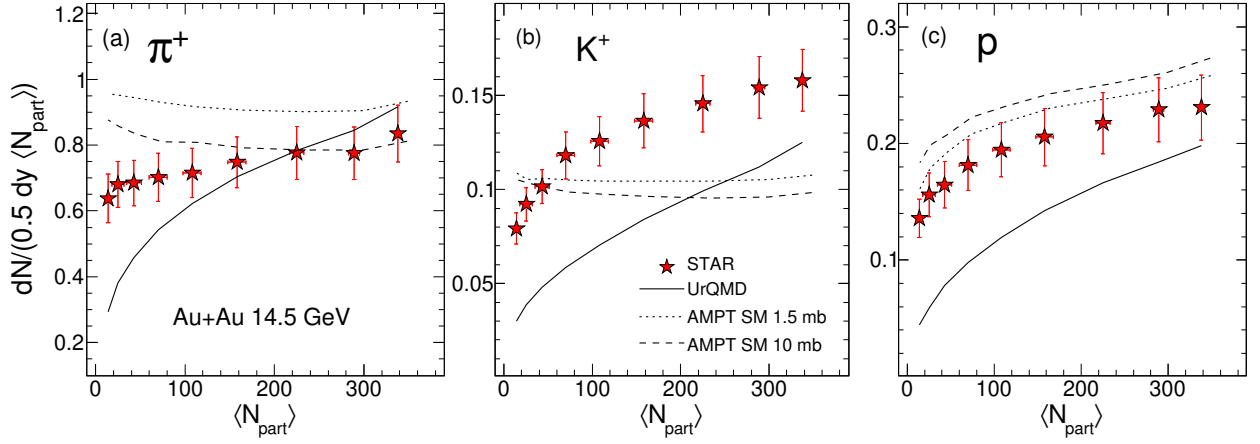

FIG. 24. $(dN/dy)/(0.5 \times \langle N_{part} \rangle)$ for π^+, K^+ and p as a function of $\langle N_{part} \rangle$ in Au+Au collisions at $\sqrt{s_{NN}} = 14.5$ GeV in STAR. These measurements are compared with UrQMD, AMPT 1.5mb and AMPT 10mb.

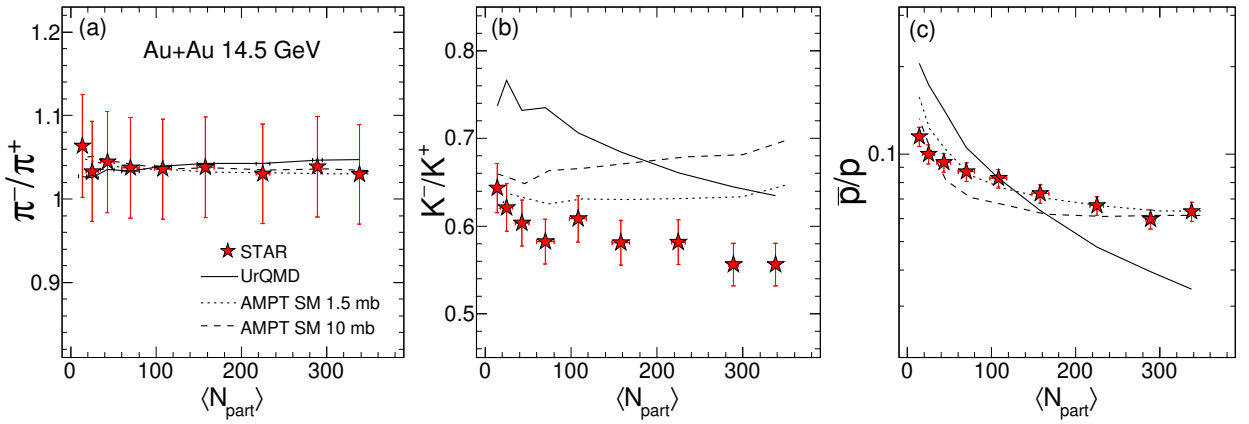FIG. 25. π^-/π^+, K^-/K^+ and $\bar{p}/p$ ratios as a function of $\langle N_{part} \rangle$ in Au+Au collisions at $\sqrt{s_{NN}} = 14.5$ GeV in STAR. These experimental ratios are compared with UrQMD, AMPT 1.5mb and AMPT 10mb.

FIG. 26. K^+/π^+, K^-/π^-, p/π^+ and $\bar{p}/\pi^-$ ratios as a function of $\langle N_{\mathrm{part}} \rangle$ in Au+Au collisions at $\sqrt{s_{\mathrm{NN}}} = 14.5$ GeV in STAR. These experimental ratios are compared with UrQMD, AMPT 1.5mb and AMPT 10mb.
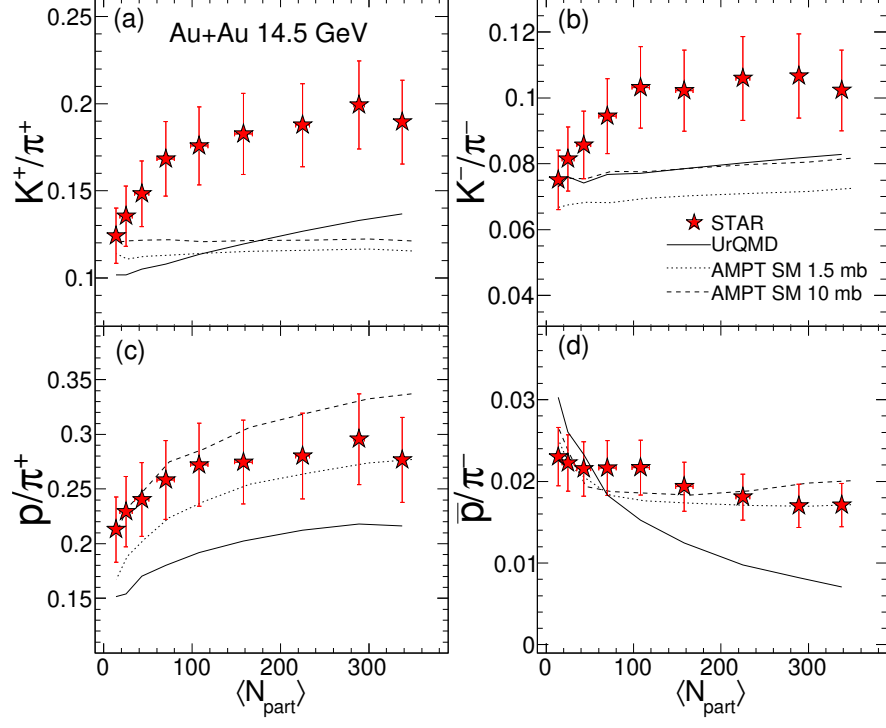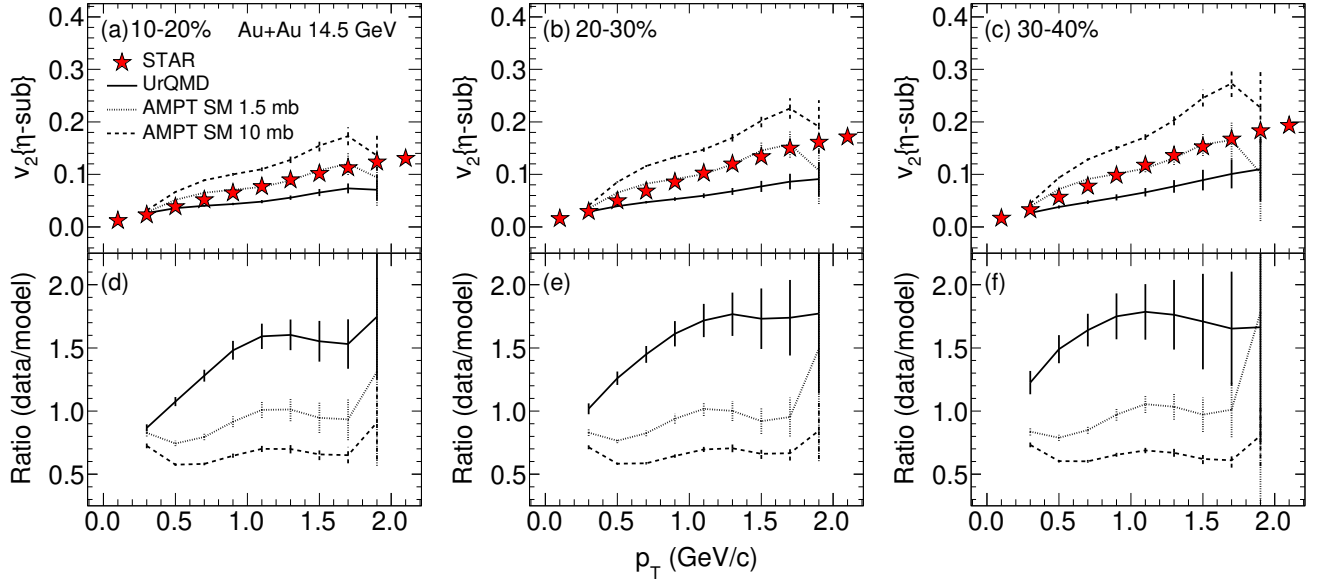

FIG. 27. Panels (a), (b), (c): p_T dependence of $v_2\{\eta-\mathrm{sub}\}$ for 14.5 GeV Au+Au collisions at 10–20%, 20–30% and 30–40% centralities, as measured by STAR. Calculations from UrQMD, AMPT 1.5mb, and AMPT 10mb are also plotted. Panels (d), (e), (f): ratios of the experimental data to each model calculation.

FIG. 28. Panels (a), (b), (c): pseudorapidity (η) dependence of $v_2\{\eta-\text{sub}\}$ for 14.5 GeV Au+Au collisions at 10–20%, 20–30% and 30–40% centralities, as measured by STAR. Calculations from UrQMD, AMPT 1.5mb, and AMPT 10mb are also plotted. Panels (d), (e), (f): ratios of the experimental data to each model calculation.
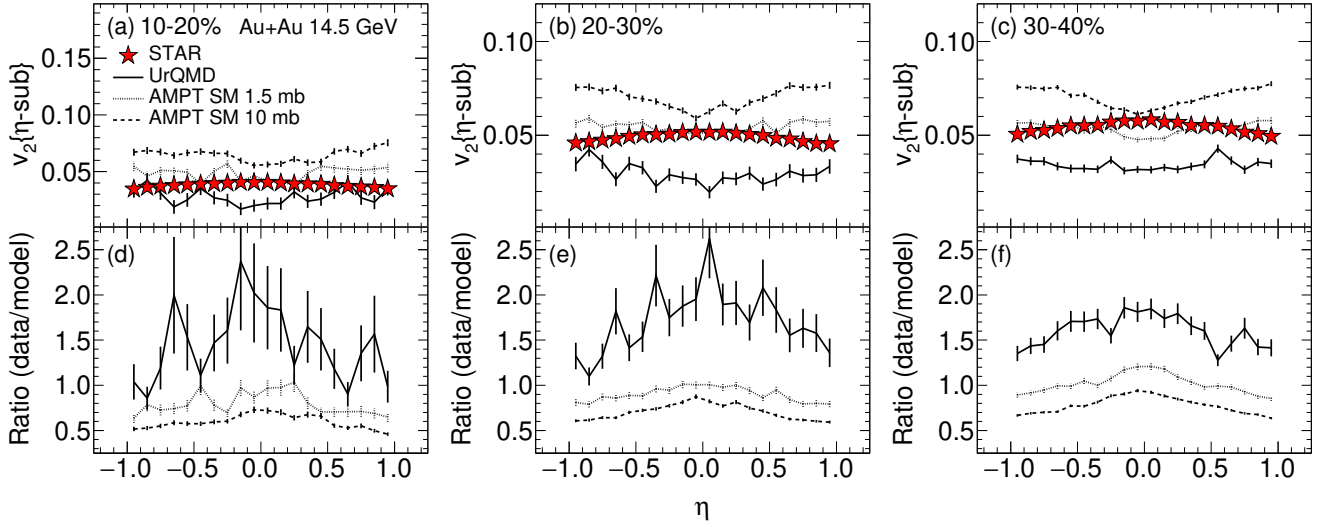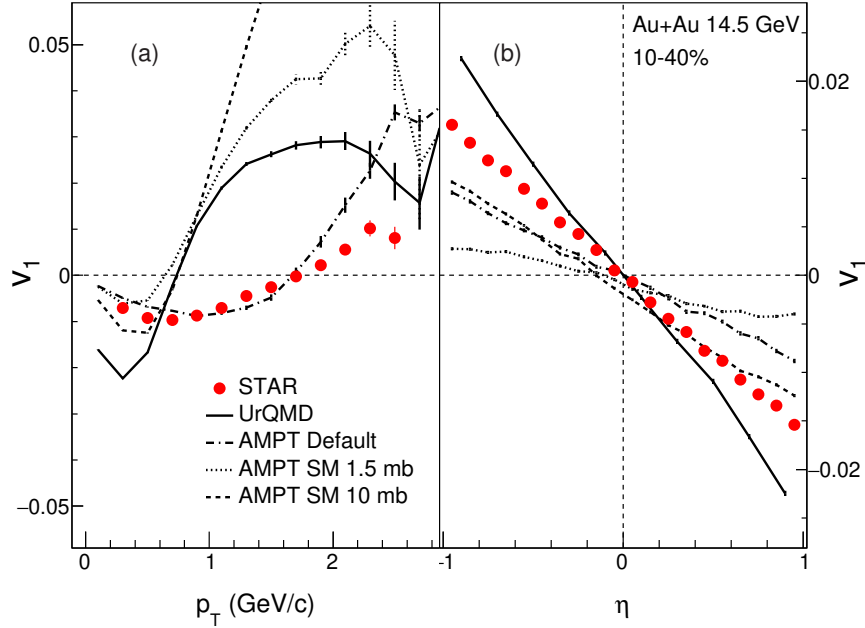

FIG. 29. Charged particle $v_1(p_T)$ (panel (a)) and $v_1(\eta)$ (panel (b)) for 10–40% centrality Au+Au collisions at $\sqrt{s_{NN}} = 14.5$ GeV. The measured directed flow is compared to UrQMD, AMPT, AMPT 1.5mb, and AMPT 10mb model calculations.

violate $v_1 = 0$ at $y = 0$, as required by symmetry. This is a known artefact of the implementation of the quark coalescence mechanism in AMPT. A recent paper has shown that this artefact can be fixed with a modified quark coalescence prescription [86].

VI. SUMMARY

We have presented basic observables for identified particles in Au+Au collisions at $\sqrt{s_{NN}} = 14.5$ GeV. The transverse momentum spectra of π, K, p, and $\bar{p}$ at midrapidity ($|y| < 0.1$) are measured for nine centralities: 0–5%, 5–10%, 10–20%, 20–30%, 30–40%, 40–50%, 50–60%, 60–70% and 70–80%. Bulk properties such as average transverse momentum $\langle p_T \rangle$, particle yields dN/dy, par-

ticle ratios, chemical and kinetic freeze-out properties, charged particle elliptic and directed flow (v_2 and v_1) are extracted for Au+Au collisions at $\sqrt{s_{NN}}$ = 14.5 GeV. All the results are compared with the published measurements at other collisions energies.

The mean $\langle p_T \rangle$ values for π, K and p increase from peripheral to central collisions – an indication of increasing radial flow in more central collisions. The centrality dependence of radial flow is more pronounced in kaons compared to pions, and in protons compared to kaons.

Midrapidity particle yields for π, K and p show a mild centrality dependence, while no dependence on centrality is observed for $\bar{p}$. The $(dN/dy)/(0.5 \times \langle N_{part} \rangle)$ for π, K and $\bar{p}$ increase with collision energy, while for p it decreases with collision energy up to 39 GeV and then increases. This effect is attributed to baryon stopping at lower RHIC energies.

No significant centrality dependence is observed in the case of π^-/π^+ and K^-/K^+ ratios. π^-/π^+ is slightly greater than unity, which is due to isospin conservation and the contribution from decays of resonances like the Δ. The $\bar{p}/p$ ratio slightly decreases from peripheral to central collisions as a consequence of increasing baryon stopping in central collisions. The K^+/π^+ and K^-/π^- ratio increases with increasing centrality and follow the energy dependence trend established at other energies. The energy dependence is due to the dominance of pair production over associated production at higher energies. The p/π^+ ratio increases from peripheral to central collisions, but no significant dependence on centrality is observed in the case of $\bar{p}/\pi^-$ ratio.

Kinetic freeze-out parameters are obtained from simultaneous Blast-Wave model fits to the p_T spectra for $\pi^\pm$, $K^\pm$ and $p(\bar{p})$. The kinetic freeze-out temperature T_k decreases from peripheral to central collisions, which is suggestive of a short-lived fireball in peripheral collisions. On the other hand, average flow velocity $\langle \beta \rangle$ increases from peripheral to central collisions, indicating larger radial flow for central collisions, consistent with $\langle p_T \rangle$ results.

The measured bulk observables are compared to UrQMD and AMPT model calculations. Values of $\langle p_T \rangle$ are underestimated by both the UrQMD and AMPT models. The AMPT model agrees with the measured dN/dy for pions ($\langle N_{part} \rangle > 100$) and protons, but does not reproduce kaon dN/dy. The UrQMD model mostly shows poor agreement with dN/dy for all the measured particles. π^-/π^+ ratios are reproduced within uncertainties by both AMPT and UrQMD models. All models show poor agreement with STAR data of K^-/K^+ and K/π ratios. The $\bar{p}/p$ ratio is well described by AMPT but not by UrQMD. The measured p/π^+ and $\bar{p}/\pi^-$ ratios are poorly reproduced by UrQMD, while AMPT does better. The dependence of v_2 of charged particles at midrapdity, on p_T and η is similar to that observed at other BES-I energies. The v_2 in peripheral collisions is larger than in central collisions. A clear centrality dependence is observed in v_2. A weak dependence of the p_T-integrated

charged particle v_2 on η is observed. The shape of $v_2(\eta)$ at 14.5 GeV resembles that reported at other beam energies.

The magnitude of charged particle v_1 increases from central to peripheral collisions at 14.5 GeV, and a similar pattern is observed at other beam energies. The magnitude of v_1 decreases with increasing beam energy.

The UrQMD model underpredicts the STAR measurement of charged particle v_2 at 14.5 GeV. The AMPT string melting option with 10 mb parton-parton interaction cross section overpredicts the data, while the 1.5 mb option is closer. The UrQMD model shows poor agreement with both $v_1(p_T)$ and $v_1(\eta)$ at 14.5 GeV.

The measured observables ($\langle p_T \rangle$, dN/dy, particle ratios, chemical and kinetic freeze-out parameters, v_2 and v_1) in Au+Au collisions at $\sqrt{s_{NN}}$ = 14.5 GeV conform to the smooth trend of beam energy dependence reported in prior publications. The results at 14.5 GeV are important since they fill the gap in μ_B of the order of about 100 MeV between beam energies 11.5 GeV and 19.6 GeV. The results will help in tuning the parameters of various models intended to explain the low energy data. Previous measurements by the STAR collaboration have revealed interesting trends related to the dominance of hadronic interaction and partonic interactions in observables such as higher moments of conserved quantities [35], v_1 [36], correlations [37], azimuthal anisotropy [38], and R_{CP} [44] between $\sqrt{s_{NN}}$ = 11.5 and 19.6 GeV. The data set at 14.5 GeV, filling a large μ_B gap, has provided a clearer understanding of the beam energy dependence of bulk observables.

Association.

[1] I. Arsene *et al.* (BRAHMS Collaboration), Nucl. Phys. A **757**, 1 (2005).

[2] K. Adcox *et al.* (PHENIX Collaboration), Nucl. Phys. A **757**, 184 (2005).

[3] B. B. Back *et al.* (PHOBOS Collaboration), Nucl. Phys. A **757**, 28 (2005).

[4] J. Adams *et al.* (STAR Collaboration), Nucl. Phys. A **757**, 102 (2005).

[5] J. Cleymans and K. Redlich, Phys. Rev. C **60**, 054908 (1999).

[6] F. Becattini, J. Manninen, and M. Gazdzicki, Phys. Rev. C **73**, 044905 (2006).

[7] A. Andronic, P. Braun-Munzinger, and J. Stachel, Nucl. Phys. A **772**, 167 (2006).

[8] J. Adams *et al.* (STAR Collaboration), Phys. Rev. Lett. **91**, 072304 (2003).

[9] J. Adams *et al.* (STAR Collaboration), Phys. Rev. Lett. **91**, 172302 (2003).

[10] B. Abelev *et al.* (STAR Collaboration), Phys. Rev. Lett. **97**, 152301 (2006).

[11] B. Abelev *et al.* (STAR Collaboration), Phys. Lett. B **655**, 104 (2007).

[12] B. Abelev *et al.* (STAR Collaboration), Phys. Rev. Lett. **99**, 112301 (2007).

[13] B. Abelev *et al.* (STAR Collaboration), Phys. Rev. C **77**, 054901 (2008).

[14] K. Rajagopal and F. Wilczek, in At the Frontier of Particle Physics/Handbook of QCD, edited by M. Shifman (World Scientific, 2001), Vol. 3, Chap. 35.

[15] F. Karsch, E. Laermann, A. Peikert, Nucl. Phys. B **605**, 579 (2001).

[16] E. Laermann and O. Philipsen, Ann. Rev. Nucl. Part. Sci. **53**, 163 (2003).

[17] M. Stephanov, PoS **LAT2006**, 024 (2006).

[18] L. Adamczyk *et al.* (STAR Collaboration), Phys. Rev. Lett. **118**, 212301 (2017).

[19] Y. Aoki, G. Endrodi, Z. Fodor, *et al.*, Nature **443**, 675 (2006).

[20] M. Cheng, N. Christ, S. Datta, *et al.*, Phys. Rev. D **77**, 014511 (2008).

[21] S. Ejiri, Phys. Rev. D **78**, 074507 (2008).

[22] M. Asakawa and K. Yazaki, Nucl. Phys. A **504**, 668 (1989).

[23] A. Barducci, R. Casalbuoni, S. De Curtis, *et al.*, Phys. Lett. B **231**, 463 (1989).

[24] A. Barducci, R. Casalbuoni, S. De Curtis, *et al.*, Phys. Rev. D **41**, 1610 (1990).

[25] M. A. Stephanov, Prog. Theor. Phys. Suppl. **153**, 139 (2004).

[26] Z. Fodor and S. Katz, JHEP **04**, 050 (2004).

[27] R. Gavai and S. Gupta, Phys. Rev. D **78**, 114503 (2008).

[28] B. Abelev *et al.* (STAR Collaboration), Phys. Rev. C **81**, 024911 (2010).

[29] B. Mohanty, Nucl. Phys. A **830**, 899c (2009).

[30] M. Aggarwal *et al.* (STAR Collaboration), arXiv:1007.2613.

[31] L. Kumar, Mod. Phys. Lett. A **28**, 1330033 (2013).

[32] L. Adamczyk *et al.*, (STAR Collaboration), Phys. Rev. C **96**, 044904 (2017).

[33] S. A. Bass *et al.*, Prog. Part. Nucl. Phys. **41**, 255 (1998); M. Bleicher *et al.*, J. Phys. G **25**, 1859 (1999).

[34] Z. W. Lin, C. M. Ko, B. A. Li, *et al.*, Phys.Rev. C **72**, 064901 (2005).

[35] L. Adamczyk *et al.* (STAR Collaboration), Phys. Rev. Lett. **112**, 032302 (2014).

[36] L. Adamczyk *et al.* (STAR Collaboration), Phys. Rev. Lett. **112**, 162301 (2014).

[37] L. Adamczyk *et al.* (STAR Collaboration), Phys. Rev. Lett. **113**, 052302 (2014).

[38] L. Adamczyk *et al.* (STAR Collaboration), Phys. Rev. Lett. **110**, 142301 (2013).

[39] L. Adamczyk *et al.* (STAR Collaboration), Phys. Rev. C **88**, 014902 (2013).

[40] L. Adamczyk *et al.* (STAR Collaboration), Phys. Rev. C **93**, 021903(R) (2016).

[41] Md. Nasim, Phys. Rev. C **89**, 034909 (2014).

[42] L. Adamczyk *et al.* (STAR Collaboration), Phys. Rev. Lett. **116**, 062301 (2016).

[43] L. Adamczyk *et al.* (STAR Collaboration), Phys. Rev. Lett. **120**, 062301 (2018).

[44] L. Adamczyk *et al.* (STAR Collaboration), Phys. Rev. Lett. **121**, 032301 (2018).

[45] K. Ackermann *et al.* (STAR Collaboration), Nucl. Instrum. Methods Phys. Res. A **499**, 624 (2003).

[46] F. Bieser, H. Crawford, J. Engelage *et al.*, Nucl. Instrum. Methods Phys. Res. A **499**, 766 (2003).

[47] C. A. Whitten (STAR Collaboration), AIP Conf. Proc. **980**, 390 (2008).

[48] M. Anderson, J. Berkovitz, W. Betts *et al.*, Nucl. Instrum. Methods Phys. Res. A **499**, 659 (2003).

[49] W. Llope, Nucl. Instrum. Methods Phys. Res. B **241**, 306 (2005).

[50] L. Adamczyk *et al.* (STAR Collaboration), Phys. Rev. C **86**, 054908 (2012).

[51] H. Bichsel, Nucl. Instrum. Methods Phys. Res. A **562**, 154 (2006).

[52] M. Aguilar-Benitez, W. Allison, A. Batalov *et al.*, Z. Phys. C **50**, 405 (1991).

[53] M. Shao *et al*, Nucl. Instrum. Methods Phys. Res. A **558**, 419 (2006).

[54] A. M. Poskanzer and S. A. Voloshin, Phys. Rev. C **58**, 1671 (1998).

[55] H. Masui, A. Schmah and A. Poskanzer, Nucl. Instrum. Methods Phys. Res. A **833**, 181 (2016).

[56] M. Nasim and B. Mohanty, Int. J. of Mod. Phys. E **24**, 1550027 (2015).

[57] G. Agakishiev *et al.* (STAR Collaboration), Phys. Rev. C **85**, 014901 (2012).

[58] A. Bilandzic, R. Snellings, and S. Voloshin, Phys. Rev. C **83**, 044913 (2011).

[59] N. Borghini, P. M. Dinh, and J.-Y. Ollitrault, Phys. Rev. C **64**, 054901 (2001).

[60] B. Abelev *et al.* (STAR Collaboration), Phys. Rev. C **79**, 034909 (2009).

[61] X.-N. Wang and M. Gyulassy, Phys. Rev. D **44**, 3501 (1991).

[62] V. Fine and P. Nevski, Proc. CHEP **2000**, 143 (2000).

[63] J. Adams *et al.* (STAR Collaboration), Phys. Rev. C **70**, 041901 (2004).

[64] M. M. Aggarwal *et al.* (STAR Collaboration), Phys. Rev. C 83, 034910 (2011).

[65] J. Adams *et al.* (STAR Collaboration), Phys. Rev. Lett. **92**, 112301 (2004).

[66] E. Schnedermann, J. Sollfrank, and Y. W. Heinz, Phys. Rev. C **48**, 2462 (1993).

[67] U. Heinz and R. Snellings, Ann. Rev. Nucl. Part. Sci. **63**, 123 (2013).

[68] X. N. Wang and M. Gyulassy, Phys. Rev. Lett. **86**, 3496 (2001).

[69] J. Randrup and J. Cleymans, Phys. Rev. C **74**, 047901 (2006).

[70] N. Xu and M. Kaneta, Nucl. Phys. A **698**, 306 (2002).

[71] J. Cleymans, B. Kampfer, M. Kaneta, S. Wheaton and N. Xu, Phys. Rev. C **71**, 054901 (2005).

[72] S. Wheaton, J. Cleymans and M. Hauer, Comput. Phys. Commun. **180**, 84 (2009).

[73] A. Andronic, F. Beutler, P. Braun-Munzinger, *et al.*, Phys. Lett. B **675**, 312 (2009).

[74] G. Wilk and Z. Wlodarczyk, Phys. Rev. Lett. **84**, 2770 (2000).

[75] B. Abelev *et al.* (ALICE Collaboration), Phys. Rev. C **88**, 044910 (2013).

[76] U. W. Heinz, arXiv:hep-ph/0407360.

[77] K. H. Ackermann *et al.*, Nucl. Instrum. Methods A **499**, 713 (2003).

[78] M. Miller, R. Snellings, arXiv:nucl-ex/0312008.

[79] M. L. Miller, K. Reygers, S. J. Sanders, and P. Steinberg, Annu. Rev. Nucl. Part. Sci. **57**, 205 (2007).

[80] J. Adams *et al.* (STAR Collaboration), Phys. Rev. C **73**, 034903 (2006).

[81] B. I. Abelev *et al.* (STAR Collaboration), Phys. Rev. Lett. **101**, 252301 (2008).

[82] K. Aamodt *et al.* (ALICE Collaboration), Phys. Rev. Lett. **105**, 252302 (2010).

[83] J. Xu and C. M. Ko, Phys. Rev. C **83**, 034904 (2011).

[84] Y. J. Ye, J. H. Chen, Y. G. Ma, S. Zhang and C. Zhong, Chin. Phys. C **41**, 084101 (2017).

[85] S. Singha, P. Shanmuganathan and D. Keane, Adv. High Energy Physics **2016**, 2836989 (2016).

[86] C.-Q. Guo, C.-J. Zhang and J. Xu, Eur. Phys. J. A **53**, 233 (2017).

APPENDIX

TABLE II. Summary of centrality bins, average number of participants N_{part}, number of binary collisions N_{coll}, reaction plane eccentricity ϵ_{RP}, participant eccentricity ϵ_{part}, root-mean-square of the participant eccentricity $\epsilon_{\mathrm{part}}\{2\}$, and transverse area S_{part} from MC Glauber simulations at $\sqrt{s_{NN}} =$14.5 GeV. The errors are systematic uncertainties.

Centrality (%)	$\langle N_{\mathrm{part}} \rangle$	$\langle N_{\mathrm{coll}} \rangle$	$\langle \epsilon_{\mathrm{RP}} \rangle$	$\langle \epsilon_{\mathrm{part}} \rangle$	$\epsilon_{\mathrm{part}}\{2\}$	$\langle S_{\mathrm{part}} \rangle$
0 − 5	338 ± 2	788 ± 30	0.04 ± 0.01	0.10 ± 0.01	0.12 ± 0.01	25.5 ± 0.6
5 − 10	289 ± 6	634 ± 20	0.11 ± 0.01	0.15 ± 0.01	0.16 ± 0.01	22.9 ± 0.7
10 − 20	226 ± 8	454 ± 24	0.18 ± 0.01	0.22 ± 0.01	0.24 ± 0.01	19.3 ± 0.8
20 − 30	159 ±10	283 ± 24	0.27 ± 0.01	0.30 ± 0.01	0.32 ± 0.01	15.5 ± 0.9
30 − 40	108 ± 10	168 ± 22	0.32 ± 0.01	0.37 ± 0.01	0.40 ± 0.01	12.4 ± 1.0
40 − 50	70 ± 8	94 ± 18	0.37 ± 0.01	0.44 ± 0.01	0.47 ± 0.01	9.8 ± 1.1
50 − 60	44 ± 8	50 ± 12	0.39 ± 0.01	0.51 ± 0.01	0.54 ± 0.01	7.6 ± 1.1
60 − 70	26 ± 7	25 ± 9	0.40 ± 0.01	0.59 ± 0.01	0.62 ± 0.01	5.6 ± 1.2
70 − 80	14 ± 5	12 ± 5	0.37 ± 0.01	0.68 ± 0.01	0.72 ± 0.01	3.5 ± 1.2

TABLE III. Track selection criteria in Au+Au collisions at $\sqrt{s_{\mathrm{NN}}} = 14.5$ GeV.

	Spectra	v_1, v_2
y/η	$|y| < 0.1$	$|\eta| < 1.0$
DCA (cm)	< 3	< 3
Number of fit points	≥ 25	≥ 15
Fraction of fit points	≥ 0.52	≥ 0.52
Number of dE/dx points	≥ 15	≥ 15

TABLE IV. dN/dy values for π^+, π^-, K^+, K^-, p, and $\bar{p}$ from Au+Au collisions at $\sqrt{s_{NN}} = 14.5$ GeV. The uncertainties represent statistical and systematic uncertainties, respectively.

Centrality(%)	π^+	π^-	K^+	K^-	p	$\bar{p}$
0 − 5	141 ± 0.2 ± 14	145 ± 0.2 ± 15	26.7 ± 0.04 ± 2.8	14.9 ± 0.03 ± 1.6	39.0 ± 0.03 ± 4.7	2.5 ± 0.02 ± 0.3
5 − 10	112 ± 0.2 ± 11	116 ± 0.1 ± 12	22.3 ± 0.04 ± 2.4	12.4 ± 0.03 ± 1.2	33.1 ± 0.03 ± 4.0	2.0 ± 0.01 ± 0.2
10 − 20	87.3 ± 0.1 ± 9.1	90.0 ± 0.1 ± 9.2	16.4 ± 0.03 ± 1.7	9.5 ± 0.02 ± 1.0	24.5 ± 0.03 ± 2.9	1.6 ± 0.01 ± 0.2
20 − 30	59.1 ± 0.1 ± 6.1	61.3 ± 0.1 ± 6.4	10.8 ± 0.02 ± 1.1	6.3 ± 0.02 ± 0.6	16.2 ± 0.02 ± 2.0	1.2 ± 0.01 ± 0.1
30 − 40	38.6 ± 0.1 ± 4.0	40.0 ± 0.1 ± 4.1	6.8 ± 0.02 ± 0.7	4.1 ± 0.01 ± 0.4	10.5 ± 0.02 ± 1.3	0.9 ± 0.01 ± 0.1
40 − 50	24.6 ± 0.1 ± 2.6	25.5 ± 0.1 ± 2.6	4.1 ± 0.01 ± 0.4	2.4 ± 0.01 ± 0.3	6.3 ± 0.01 ± 0.8	0.60 ± 0.004 ± 0.07
50 − 60	14.7 ± 0.04 ± 1.5	15.4 ± 0.04 ± 1.5	2.2 ± 0.01 ± 0.2	1.3 ± 0.01 ± 0.1	3.5 ± 0.01 ± 0.4	0.33 ± 0.003 ± 0.04
60 − 70	8.5 ± 0.03 ± 0.9	8.8 ± 0.03 ± 0.9	1.2 ± 0.01 ± 0.1	0.72 ± 0.01 ± 0.07	1.9 ± 0.01 ± 0.2	0.16 ± 0.003 ± 0.02
70 − 80	4.5 ± 0.03 ± 0.5	4.8 ± 0.03 ± 0.6	0.55 ± 0.01 ± 0.06	0.36 ± 0.01 ± 0.04	0.6 ± 0.01 ± 0.1	0.11 ± 0.002 ± 0.01

TABLE V. The $\langle p_{\mathrm{T}} \rangle$ (MeV/c) values for π^+, π^-, K^+, K^-, p, and $\bar{p}$ from Au+Au collisions at $\sqrt{s_{NN}} = 14.5$ GeV. The uncertainties represent statistical and systematic uncertainties, respectively.

Centra-lity(%)	π^+	π^-	K^+	K^-	p	$\bar{p}$
$0-5$	$395 \pm 0.1 \pm 22$	$392 \pm 0.1 \pm 21$	$586 \pm 0.1 \pm 32$	$560 \pm 0.1 \pm 30$	$811 \pm 0.1 \pm 53$	$807 \pm 0.2 \pm 69$
$5-10$	$393 \pm 0.1 \pm 22$	$390 \pm 0.1 \pm 21$	$575 \pm 0.1 \pm 32$	$559 \pm 0.1 \pm 30$	$798 \pm 0.1 \pm 52$	$800 \pm 0.2 \pm 68$
$10-20$	$393 \pm 0.2 \pm 22$	$388 \pm 0.2 \pm 21$	$574 \pm 0.1 \pm 32$	$552 \pm 0.1 \pm 30$	$781 \pm 0.1 \pm 51$	$776 \pm 0.2 \pm 66$
$20-30$	$389 \pm 0.2 \pm 21$	$384 \pm 0.2 \pm 20$	$560 \pm 0.2 \pm 31$	$540 \pm 0.1 \pm 29$	$765 \pm 0.1 \pm 50$	$751 \pm 0.3 \pm 64$
$30-40$	$382 \pm 0.2 \pm 21$	$380 \pm 0.2 \pm 20$	$555 \pm 0.2 \pm 31$	$532 \pm 0.1 \pm 29$	$730 \pm 0.1 \pm 48$	$726 \pm 0.3 \pm 62$
$40-50$	$374 \pm 0.3 \pm 21$	$374 \pm 0.3 \pm 20$	$530 \pm 0.2 \pm 29$	$513 \pm 0.1 \pm 28$	$686 \pm 0.1 \pm 45$	$675 \pm 0.4 \pm 57$
$50-60$	$365 \pm 0.3 \pm 20$	$366 \pm 0.3 \pm 19$	$518 \pm 0.3 \pm 29$	$495 \pm 0.2 \pm 27$	$646 \pm 0.1 \pm 42$	$640 \pm 0.4 \pm 54$
$60-70$	$356 \pm 0.4 \pm 20$	$355 \pm 0.4 \pm 19$	$496 \pm 0.4 \pm 27$	$475 \pm 0.2 \pm 26$	$627 \pm 0.1 \pm 40$	$606 \pm 0.1 \pm 52$
$70-80$	$349 \pm 1 \pm 19$	$347 \pm 1 \pm 18$	$484 \pm 1 \pm 27$	$460 \pm 1 \pm 25$	$587 \pm 2 \pm 38$	$573 \pm 1 \pm 49$

TABLE VI. Kinetic freeze-out parameters T_k, $\langle \beta \rangle$, n and χ^2/ndf values from Blast-Wave fits in Au+Au collisions at $\sqrt{s_{NN}} = 14.5$ GeV. The quoted errors are total statistical and systematic uncertainties added in quadrature.

Centrality(%)	T_k (MeV)	$\langle \beta \rangle$	n	χ^2/ndf
$0-5$	114 ± 7	0.485 ± 0.036	0.97 ± 0.28	0.119
$5-10$	116 ± 7	0.442 ± 0.035	0.98 ± 0.29	0.097
$10-20$	118 ± 7	0.429 ± 0.034	0.99 ± 0.33	0.119
$20-30$	122 ± 7	0.401 ± 0.034	1.00 ± 0.39	0.056
$30-40$	124 ± 8	0.371 ± 0.042	1.34 ± 0.42	0.123
$40-50$	130 ± 6	0.312 ± 0.036	1.73 ± 0.61	0.232
$50-60$	134 ± 6	0.238 ± 0.031	2.26 ± 0.78	0.398
$60-70$	136 ± 6	0.194 ± 0.030	2.76 ± 0.87	0.484
$70-80$	139 ± 7	0.168 ± 0.030	2.83 ± 1.20	0.354

TABLE VII. Inclusive charged particle v_1 as function of p_{T} in Au+Au collisions at $\sqrt{s_{NN}} = 14.5$ GeV. The uncertainties represent statistical and systematic uncertainties, respectively.

p_{T} (GeV/c)	v_1(0–10%)	v_1 (10–40%)	v_1 (40–80%)
0.30	$-0.0027 \pm 0.0003 \pm 0.0001$	$-0.0071 \pm 0.0001 \pm 0.0004$	$-0.0130 \pm 0.0002 \pm 0.0007$
0.50	$-0.0034 \pm 0.0003 \pm 0.0002$	$-0.0093 \pm 0.0001 \pm 0.0005$	$-0.0176 \pm 0.0002 \pm 0.0008$
0.70	$-0.0032 \pm 0.0004 \pm 0.0002$	$-0.0096 \pm 0.0001 \pm 0.0004$	$-0.0201 \pm 0.0003 \pm 0.0009$
0.90	$-0.0024 \pm 0.0006 \pm 0.0003$	$-0.0087 \pm 0.0002 \pm 0.0003$	$-0.0216 \pm 0.0004 \pm 0.0010$
1.10	$0.0014 \pm 0.0008 \pm 0.0005$	$-0.0070 \pm 0.0003 \pm 0.0004$	$-0.0219 \pm 0.0006 \pm 0.0007$
1.30	$0.0019 \pm 0.0010 \pm 0.0005$	$-0.0045 \pm 0.0003 \pm 0.0001$	$-0.0226 \pm 0.0008 \pm 0.0005$
1.50	$0.0047 \pm 0.0014 \pm 0.0007$	$-0.0025 \pm 0.0005 \pm 0.0003$	$-0.0209 \pm 0.0011 \pm 0.0009$
1.70	$0.0040 \pm 0.0019 \pm 0.0007$	$-0.0002 \pm 0.0006 \pm 0.0003$	$-0.0185 \pm 0.0016 \pm 0.0008$
1.90	$0.0079 \pm 0.0026 \pm 0.0007$	$0.0024 \pm 0.0009 \pm 0.0003$	$-0.0179 \pm 0.0023 \pm 0.0008$
2.10	$0.0095 \pm 0.0036 \pm 0.0014$	$0.0059 \pm 0.0012 \pm 0.0004$	$-0.0173 \pm 0.0032 \pm 0.0013$
2.30	$0.0155 \pm 0.0050 \pm 0.0021$	$0.0097 \pm 0.0017 \pm 0.0007$	$-0.0125 \pm 0.0046 \pm 0.0015$
2.50	$0.0089 \pm 0.0069 \pm 0.0024$	$0.0081 \pm 0.0024 \pm 0.0007$	$-0.0067 \pm 0.0065 \pm 0.0024$

TABLE VIII. Inclusive charged particle v_1 as function of η in Au+Au collisions at $\sqrt{s_{NN}}$ = 14.5 GeV. The uncertainties represent statistical and systematic uncertainties, respectively.

η	v_1 (0–10%)	v_1 (10–40%)	v_1 (40–80%)
−0.95	$0.0059 \pm 0.0008 \pm 0.0007$	$0.0157 \pm 0.0003 \pm 0.0005$	$0.0334 \pm 0.0006 \pm 0.0000$
−0.85	$0.0048 \pm 0.0008 \pm 0.0006$	$0.0137 \pm 0.0003 \pm 0.0003$	$0.0295 \pm 0.0005 \pm 0.0000$
−0.75	$0.0034 \pm 0.0008 \pm 0.0003$	$0.0119 \pm 0.0002 \pm 0.0001$	$0.0258 \pm 0.0005 \pm 0.0000$
−0.65	$0.0030 \pm 0.0007 \pm 0.0003$	$0.0108 \pm 0.0002 \pm 0.0001$	$0.0211 \pm 0.0005 \pm 0.0000$
−0.55	$0.0019 \pm 0.0007 \pm 0.0003$	$0.0089 \pm 0.0002 \pm 0.0001$	$0.0186 \pm 0.0005 \pm 0.0000$
−0.45	$0.0015 \pm 0.0007 \pm 0.0003$	$0.0073 \pm 0.0002 \pm 0.0001$	$0.0137 \pm 0.0005 \pm 0.0000$
−0.35	$0.0032 \pm 0.0007 \pm 0.0003$	$0.0054 \pm 0.0002 \pm 0.0000$	$0.0111 \pm 0.0005 \pm 0.0002$
−0.25	$0.0015 \pm 0.0007 \pm 0.0003$	$0.0043 \pm 0.0002 \pm 0.0001$	$0.0083 \pm 0.0005 \pm 0.0001$
−0.15	$0.0015 \pm 0.0007 \pm 0.0006$	$0.0026 \pm 0.0002 \pm 0.0001$	$0.0049 \pm 0.0005 \pm 0.0001$
−0.05	$0.0007 \pm 0.0007 \pm 0.0004$	$0.0005 \pm 0.0002 \pm 0.0001$	$0.0013 \pm 0.0005 \pm 0.0001$
0.05	$-0.0004 \pm 0.0007 \pm 0.0003$	$-0.0007 \pm 0.0002 \pm 0.0001$	$-0.0025 \pm 0.0005 \pm 0.0002$
0.15	$-0.0008 \pm 0.0007 \pm 0.0003$	$-0.0028 \pm 0.0002 \pm 0.0001$	$-0.0051 \pm 0.0005 \pm 0.0001$
0.25	$-0.0013 \pm 0.0007 \pm 0.0004$	$-0.0045 \pm 0.0002 \pm 0.0001$	$-0.0072 \pm 0.0005 \pm 0.0001$
0.35	$-0.0011 \pm 0.0007 \pm 0.0002$	$-0.0058 \pm 0.0002 \pm 0.0001$	$-0.0123 \pm 0.0005 \pm 0.0001$
0.45	$-0.0009 \pm 0.0007 \pm 0.0003$	$-0.0078 \pm 0.0002 \pm 0.0002$	$-0.0151 \pm 0.0005 \pm 0.0002$
0.55	$-0.0035 \pm 0.0007 \pm 0.0003$	$-0.0088 \pm 0.0002 \pm 0.0002$	$-0.0182 \pm 0.0005 \pm 0.0003$
0.65	$-0.0029 \pm 0.0007 \pm 0.0003$	$-0.0107 \pm 0.0002 \pm 0.0001$	$-0.0230 \pm 0.0005 \pm 0.0001$
0.75	$-0.0034 \pm 0.0008 \pm 0.0003$	$-0.0123 \pm 0.0002 \pm 0.0000$	$-0.0255 \pm 0.0005 \pm 0.0002$
0.85	$-0.0041 \pm 0.0008 \pm 0.0008$	$-0.0134 \pm 0.0002 \pm 0.0001$	$-0.0285 \pm 0.0005 \pm 0.0004$
0.95	$-0.0027 \pm 0.0008 \pm 0.0007$	$-0.0154 \pm 0.0003 \pm 0.0002$	$-0.0338 \pm 0.0006 \pm 0.0005$